The Astrophysical Journal, 761:89 (23pp), 2012 December 20
Preprint typeset using LaTeX style emulateapj v. 12/16/11

arXiv:1209.1626v2 [astro-ph.CO] 7 Jan 2013

# PRECISE IDENTIFICATIONS OF SUBMILLIMETER GALAXIES: MEASURING THE HISTORY OF MASSIVE STAR-FORMING GALAXIES TO $Z > 5$[1,2,3]

A. J. Barger[4,5,6], W.-H. Wang[7], L. L. Cowie[6], F. N. Owen[8], C.-C. Chen[6], J. P. Williams[6]

*The Astrophysical Journal, 761:89 (23pp), 2012 December 20*

## ABSTRACT

We carried out extremely sensitive Submillimeter Array (SMA) 340 GHz (860 $\mu$m) continuum imaging of a complete sample of SCUBA 850 $\mu$m sources ($> 4\sigma$) with fluxes $> 3$ mJy in the GOODS-N. Using these data and new SCUBA-2 data, we do not detect 4 of the 16 SCUBA sources, and we rule out the original SCUBA fluxes at the $4\sigma$ level. Three more resolve into multiple fainter SMA galaxies, suggesting that our understanding of the most luminous high-redshift dusty galaxies may not be as reliable as we thought. 10 of the 16 independent SMA sources have spectroscopic redshifts (optical/infrared or CO) to $z = 5.18$. Using a new, ultradeep 20 cm image obtained with the Karl G. Jansky Very Large Array (rms of 2.5 $\mu$Jy), we find that all 16 of the SMA sources are detected at $> 5\sigma$. Using *Herschel* far-infrared (FIR) data, we show that the five isolated SMA sources with *Herschel* detections are well described by an Arp 220 spectral energy distribution template in the FIR. They also closely obey the local FIR-radio correlation, a result that does not suffer from a radio bias. We compute the contribution from the 16 SMA sources to the universal star formation rate per comoving volume. With individual star formation rates in the range $700 - 5000$ $M_\odot$ yr$^{-1}$, they contribute $\sim 30\%$ of the extinction-corrected ultraviolet selected star formation rate density from $z = 1$ to at least $z = 5$. Star formation histories determined from extinction-corrected ultraviolet populations and from submillimeter galaxy populations only partially overlap, due to the extreme ultraviolet faintness of some submillimeter galaxies.

*Subject headings:* cosmology: observations — galaxies: abundances — galaxies: distances and redshifts — galaxies: evolution — galaxies: starburst

## 1. INTRODUCTION

The detection of the far-infrared (FIR) extragalactic background light (EBL) by *COBE* (e.g., Puget et al. 1996; Fixsen et al. 1998; Hauser et al. 1998) was soon followed by the resolution of the bulk of the EBL at 850 $\mu$m into discrete sources through deep submillimeter surveys with the Submillimeter Common-User Bolometer Array (SCUBA; Holland et al. 1999) on the single-dish James Clerk Maxwell Telescope (JCMT) 15 m (e.g., Smail et al. 1997; Barger et al. 1998, 1999; Hughes et al. 1998; Eales et al. 1999, 2000; Blain et al. 1999; Cowie et al. 2002; Scott et al. 2002; Webb et al. 2003; Borys et al. 2003; Serjeant et al. 2003; Wang et al. 2004; Pope et al. 2005; Coppin et al. 2006; Knudsen et al. 2008). Millimeter continuum surveys were also undertaken using the AzTEC (1.1 mm) bolometric camera (Wilson et al. 2008) on both the JCMT (e.g., Scott et al. 2008; Perera et al. 2008; Austermann et al. 2010; Michałowski et al. 2012) and the Atacama Submillimeter Telescope Experiment (ASTE; Ezawa et al. 2004) 10 m (e.g., Aretxaga et al. 2011; Scott et al. 2010, 2012; Yun et al. 2012) and using the Max-Planck Millimeter Bolometer (MAMBO; Kreysa et al. 1998) array (1.2 mm) on the Institut de Radioastronomie Millimétrique (IRAM) 30 m telescope (e.g., Dannerbauer et al. 2004; Grève et al. 2004, 2008; Bertoldi et al. 2007; Lindner et al. 2011). Most recently, additional submillimeter surveys have been done at 870 $\mu$m using the Large APEX Bolometer Camera (LABOCA; Siringo et al. 2009) on the Atacama Pathfinder Experiment (APEX; Güsten et al. 2006) 12 m telescope (e.g., Weiß et al. 2009; Johansson et al. 2011; Wardlow et al. 2011).

Through all of this work, we have learned that a large fraction of cosmic star formation is hidden by dust (e.g., Barger et al. 2000; Lagache et al. 2005; Chapman et al. 2005; Wang et al. 2006; Serjeant et al. 2008), and hence that the construction of a complete picture of galaxy evolution also requires an understanding of FIR and submillimeter galaxies (SMGs). However, the challenge in studying the properties of this important population of galaxies in detail has always been the low resolution of the FIR/submillimeter/millimeter data, which makes it difficult to identify the correct counterparts and to carry out follow-up observations.

One popular approach for pinpointing SMGs has been to use deep radio interferometric images. This approach takes advantage of the well-known tight empirical corre-

[1] The Submillimeter Array is a joint project between the Smithsonian Astrophysical Observatory and the Academia Sinica Institute of Astronomy and Astrophysics and is funded by the Smithsonian Institution and the Academia Sinica.
[2] The National Radio Astronomy Observatory is a facility of the National Science Foundation operated under cooperative agreement by Associated Universities, Inc.
[3] Herschel is an ESA space observatory with science instruments provided by European-led Principal Investigator consortia and with important participation from NASA.
[4] Department of Astronomy, University of Wisconsin-Madison, 475 N. Charter Street, Madison, WI 53706.
[5] Department of Physics and Astronomy, University of Hawaii, 2505 Correa Road, Honolulu, HI 96822.
[6] Institute for Astronomy, University of Hawaii, 2680 Woodlawn Drive, Honolulu, HI 96822.
[7] Academia Sinica Institute of Astronomy and Astrophysics, P.O. Box 23-141, Taipei 10617, Taiwan
[8] National Radio Astronomy Observatory, P.O. Box O, Socorro, NM 87801.

lation between non-thermal radio emission and thermal dust emission (e.g., Helou et al. 1985; Condon 1992). Indeed, about 60%−70% of bright ($S_{850\ \mu\mathrm{m}} \gtrsim 5$ mJy) SMGs are found to have radio counterparts above 20 cm flux limits of $\sim 30$ $\mu$Jy (e.g., Barger et al. 2000; Ivison et al. 2002; Chapman et al. 2003b). With the subarcsec positional accuracy of the radio data, it has been possible to follow up a number of these bright SMGs spectroscopically. Chapman et al. (2003a, 2005) found a redshift distribution between $z \sim 1.5 - 3.5$ for these sources.

We note in passing that mid-infrared (MIR) data from *Spitzer* are also commonly used to identify counterparts to SMGs (e.g., Pope et al. 2006), but the resolution of these data is lower ($\sim 2''$ resolution for IRAC; the 24 $\mu$m MIPS catalogs usually require IRAC source positions as priors) than in the radio. More recently, *Herschel*-PACS data (beam sizes of $6\farcs7$ and $11\farcs0$ at 100 $\mu$m and 160 $\mu$m, respectively) have been used (e.g., Dannerbauer et al. 2010). Finally, hard X-ray observations with *Chandra* can also identify dusty active galactic nuclei (AGNs) (e.g., Bautz et al. 2000; Severgnini et al. 2000; Barger et al. 2001a,b; Alexander et al. 2003a).

Unfortunately, there are several drawbacks to using radio emission to identify SMGs. First, with the current sensitivity of radio interferometers ($5\sigma$ of $\sim 20$ $\mu$Jy at 20 cm prior to the upgrade of the Karl G. Jansky Very Large Array or VLA, e.g., Fomalont et al. 2006; Owen & Morrison 2008; Morrison et al. 2010; Wold et al. 2012; and now $5\sigma$ of $\sim 12.5$ $\mu$Jy with the upgrade, e.g., F. Owen et al. 2013, in preparation; hereafter, Owen13), the radio-identified SMGs are mostly bright in the submillimeter, so their properties may not be representative of SMGs as a whole. Second, the radio flux drops at high redshifts due to the positive $K$-correction of the radio synchrotron emission, while the submillimeter flux remains almost invariant over the redshift range $z \sim 1-8$ (Blain & Longair 1993) due to the negative $K$-correction of the submillimeter thermal dust emission. Compton cooling on the cosmic microwave background (CMB) radiation may also significantly reduce the 20 cm emission in the highest redshift sources (Condon 1992). Thus, the radio identification technique is biased against high-redshift sources. Finally, a number of SMGs have been found to have more than one candidate radio counterpart (e.g., Ivison et al. 2002, 2007; Pope et al. 2006), making identifying the correct counterpart to the SMG or determining whether there may be multiple counterparts difficult.

High-resolution interferometric imaging at the wavelength of the original detection is clearly a more reliable way to identify the correct counterparts to SMGs. It is also a way to confirm that an SMG is real rather than a false positive. This is particularly important when counterparts at other wavelengths cannot be found, since then the source could be interpreted as being at a very high redshift when it is in fact not real.

Observations with the Submillimeter Array (SMA; Ho et al. 2004) have proven to be very useful for localizing the submillimeter emission from SCUBA sources (e.g., Iono et al. 2006; Wang et al. 2007, 2011; Younger et al. 2008; Cowie et al. 2009; Hatsukade et al. 2010; Knudsen et al. 2010; Chen et al. 2011), as have millimeter observations with the IRAM Plateau de Bure Interferometer (PdBI) using either continuum emission (e.g., Downes et al. 1999; Dannerbauer et al. 2008) or CO molecular line emission (e.g., Daddi et al. 2009a,b; Walter et al. 2012). Indeed, through the above studies of the SCUBA sources and other studies made using various telescope and instrument combinations (e.g., Capak et al. 2008, 2011; Schinnerer et al. 2008; Coppin et al. 2009, 2010; Riechers et al. 2010; Smolčić et al. 2011), the redshift distribution of SMGs has now been extended to $z > 5$.

Moreover, the SMA observations have successfully discriminated between multiple plausible counterparts identified at other wavebands. For example, in several cases, only one of the multiple candidate radio counterparts was found to be the source of the submillimeter emission (Younger et al. 2007, 2008, 2009; Hatsukade et al. 2010).

However, perhaps the most interesting and important result to come out of the limited number of existing SMA interferometric localizations is the discovery that some of the brighter SCUBA sources resolve into multiple, physically unrelated SMGs (Wang et al. 2011). The Wang et al. results reinforce the notion that cross-identifications of the dusty galaxies at any wavelength other than the submillimeter can be misleading, since such identifications are typically based on only one of the real counterparts. Thus, the redshift distribution of the dusty star formation may need to be revised.

For the last few years, we have been observing with the SMA the $> 4\sigma$ sample of SCUBA-identified SMGs with 850 $\mu$m fluxes $> 3$ mJy in the Great Observatories Origins Deep Survey-North (GOODS-N; Giavalisco et al. 2004) presented by Wang et al. (2004; hereafter, W04; see their Table 1). There are 16 such sources listed in the W04 table. Most of these sources are also in the SCUBA Super-map catalog of Pope et al. (2005; see their Table A1). W04 used the naming convention (prefix) GOODS 850, while P05 used the naming convention (prefix) GN for GOODS-N. In addition, some of the sources in the Hubble Deep Field-North proper (HDF-N; Williams et al. 1996) appeared in the Hughes et al. (1998) discovery paper, where they used the naming convention (prefix) HDF 850. For clarity and ease of comparison with the literature, where there are overlaps, we always give all relevant names.

Note that the reason we imposed the $> 3$ mJy flux limit is because anything fainter than this is too hard to do with the sensitivity of the SMA. Applying this flux limit only removed GOODS 850-10 (GN 13 or HDF 850.4) from the $4\sigma$ sample of W04, where it is listed as having a SCUBA flux of $2.6 \pm 0.5$ mJy.

Many recent analyses have focused on large samples of submillimeter or millimeter galaxies, which usually come at the expense of being heterogeneously selected, not uniformly of high significance, and often without high-resolution submillimeter or millimeter imaging. As a consequence, some of the sources may not be real or may have overestimated submillimeter fluxes, while others may be multiples and/or have their counterparts misidentified. It is well-known in the literature that using lower significance thresholds is very dangerous due to the increased contamination from flux boosting (e.g., Eddington 1913; Eales et al. 2000; Scott et al. 2002; Wang et al. 2004). Moreover, as shown by Wang et al. (2011), multiple sources can blend in single-dish observations to form a single, apparently more luminous source[1], the

components of which may not even be physically related.

These recent analyses are orthogonal to the philosophy of the present paper, which is to concentrate on an extremely well-understood sample of uniformly selected SMGs at the expense of the sample being relatively small. Here we analyze our targeted SMA sample as a whole. We have already published a few of our SMA sources in previous work. In Wang et al. (2011), we presented GOODS 850-11 (GN 12) and GOODS 850-13 (GN 21), which we found to be composed of two and three distinct and unrelated sources, respectively. In Cowie et al. (2009), we presented GOODS 850-1 (GN14 or HDF 850.1), which continues to elude detection at optical/near-infrared (NIR) wavelengths but now has a redshift of $z = 5.183$ from millimeter spectroscopy (Walter et al. 2012). In Wang et al. (2007), we presented GOODS 850-5 (GN 10), which is also undetected at optical/NIR wavelengths (Wang et al. 2009) but now has a redshift of $z \sim 4.05$ from millimeter spectroscopy (Daddi et al. 2009a).

Aiding our analysis, L. Cowie et al. (2013, in preparation; hereafter, C13) recently obtained a 6 hr observation of the GOODS-N field in band 2 weather (225 GHz opacity $\sim 0.05 - 0.08$) using SCUBA-2 on the JCMT, providing a uniform sample over the field to $\sim 8$ mJy ($4\sigma$). SCUBA-2 is the most powerful camera for observing light at submillimeter wavelengths. It covers 16 times the area of SCUBA and has a mapping speed that is considerably faster than SCUBA at both 850 $\mu$m and 450 $\mu$m. The arrays sample the sky in a way that is akin to CCDs or infrared cameras. The angular resolution of SCUBA-2 on the sky is a lot better than that of the space-based missions. For example, at the *Herschel* satellite's longest wavelength (500 $\mu$m), the beam FWHM size is $\sim 35''$, whereas the beam FWHM sizes of SCUBA-2 are $\sim 7.5''$ and $\sim 14''$ at 450 $\mu$m and 850 $\mu$m, respectively. The SCUBA-2 data provide an independent test of the reliability of the high-significance SCUBA samples in this field.

Also aiding our analysis, Owen13 recently obtained a 39 hr observation of the GOODS-N field at 20 cm with the upgraded VLA. This image reaches an rms of 2.5 $\mu$Jy. All of the galaxies in our SMA sample are detected in this image. Moreover, because of the high spatial resolution of both the submillimeter and radio images, the positions of the galaxies, and the cross-identifications of the submillimeter and radio sources, are unambiguous. We use the combination of the submillimeter and radio measurements to estimate millimetric redshifts for the galaxies without spectroscopic redshifts. We note that many of the galaxies without spectroscopic redshifts are faint in the optical/NIR, making the use of photometric redshifts challenging. We also use the combined data to determine $q$ values ($q$ is a measure of the logarithmic FIR/radio fux density ratio; e.g., Condon et al. 1991) in order to search for signs of evolution with FIR luminosity or redshift. Finally, we determine the radio luminosities for the galaxies, which we use to estimate the cosmic star formation history.

In Section 2, we present our SMA observations and data reduction. In Section 3, we establish our SMA sample, eliminating the sources in the original SCUBA sample that we do not detect with the SMA and SCUBA-2. In Section 4, we analyze the sources in the sample, including determining the rate of multiplicity, the radio properties, the redshifts (spectroscopic and/or millimetric), and the optical/NIR properties. In Section 5, we construct spectral energy distributions for the 5 SMGs in our SMA sample that are isolated and have *Herschel* detections. These SMGs have sufficient wavelength coverage over the peak of the thermal dust spectrum to constrain the quantity $q$. We include an additional source at $z = 5.183$, whose 860 $\mu$m flux is close enough to the peak to provide strong constraints on $q$, to look for evolution in the high-redshift FIR-radio correlation to redshifts beyond 5. In Section 6, we use our SMA sample to construct the star formation rate density over the redshift range $z = 1 - 6$. In Section 7, we summarize our results. We adopt the AB magnitude system for the optical and NIR photometry, and we assume the Wilkinson Microwave Anisotropy Probe cosmology of $H_0 = 70.5$ km s$^{-1}$ Mpc$^{-1}$, $\Omega_{\rm M} = 0.27$, and $\Omega_\Lambda = 0.73$ (Larson et al. 2011) throughout.

## 2. SMA OBSERVATIONS AND DATA REDUCTION

As we discussed in the introduction, we targeted with the SMA W04's $> 4\sigma$ sample of SCUBA-identified SMGs with 850 $\mu$m fluxes $> 3$ mJy in the GOODS-N. In Table 1, we give the details of our SMA observations of each source. The only source in the sample of 16 that we did not observe with the SMA was GOODS850-14, which is not detected in the SCUBA-2 observations (see Section 3). The upgrade of the SMA to a 4 GHz bandwidth during the course of our observing program considerably improved the continuum sensitivity and made calibrations with fainter quasars easier. In Column 1, we give the W04 name for the SCUBA source, followed by the P05 and Hughes et al. (1998) names, where available; in Column 2, the date of the observation; in Column 3, the system temperature (this contains everything related to the sensitivity, including the opacity, the phase stability caused by air, and the instrument); in Column 4, the exposure time on source; in Column 5, the number of antennas used; in Column 6, the passband of the observations (we give the frequency center followed by the frequency range for each side band, where the latter is the same number for both side bands); in Column 7, the beam size; in Column 8, the beam position angle; in Column 9, the flux calibrator(s); in Column 10, the passband calibrator(s); and in Column 11, the complex gain calibrators. The observed frequencies range from 340 to 350 GHz (850-880 $\mu$m), and we label them as 860 $\mu$m.

We performed the calibration and data inspection using the IDL-based Caltech package MIR modified for the

[1] We note that after this paper was submitted, Karim et al. (2012) presented Atacama Large Millimeter Array (ALMA) observations of a large sample of 870 $\mu$m selected submillimeter sources from the LABOCA Extended *Chandra* Deep South Submillimeter Survey (LESS). They found no ALMA sources with fluxes $> 9$ mJy. They also found that all of the ALMA-observed $> 12$ mJy sources in the original LESS observations were composed of emission from multiple, fainter SMGs. Both results are more extreme than presented here: we see three single SMA sources with fluxes $> 9$ mJy and confirm two of the three $> 12$ mJy sources in the original SCUBA observations as being single sources based on the SMA data.

TABLE 1
SMA Observations

| Name GOODS | Name GN/HDF | Date | $T_{sys}$ | Exp. | # Ant. | Passband[a] | Beam Size | Beam PA | Flux Calibrator(s) | Passband Calibrator(s) | Complex Gain Calibrators |
|---|---|---|---|---|---|---|---|---|---|---|---|
| | | | (K) | (hr) | | (GHz) | ($''\times''$) | (deg) | | | |
| (1) | | (2) | (3) | (4) | (5) | (6) | (7) | (8) | (9) | (10) | (11) |
| 850-1[b] | 14/850.1 | 20080224 | 420 | 6.0 | 8 | 350, 2 | $2.09 \times 1.76$[d] | 60.2[d] | Ceres, Callisto | 3c111 | 1048+717, 1419+543 |
| 850-1[c] | 14/850.1 | 20080421 | 610 | 5.9 | 7 | 340, 2 | | | Callisto | 3c454.3 | 1048+717, 1419+543 |
| 850-2 | 09 | 20090505 | 350 | 3.5 | 7 | 340, 2 | $2.08 \times 1.28$ | 64.6 | Callisto | 3c273 | 1058+812, 1642+689 |
| 850-3 | 06 | 20110424 | 340 | 4.6 | 8 | 342, 4 | $2.22 \times 2.12$ | -66.2 | Neptune | 3c454.3 | 1153+495, 1642+689 |
| 850-4 | ··· | 20070215 | 630 | 6.9 | 7 | 340, 2 | $2.32 \times 1.33$ | 49.6 | Callisto | 3c84 | 1048+717, 1419+543 |
| 850-5 | 10 | 20070123 | 380 | 6.6 | 8 | 340, 2 | $2.42 \times 2.19$ | 24.3 | Callisto | 3c84 | 1048+717, 1419+543 |
| 850-6 | ··· | 20110325 | 430 | 8.1 | 8 | 342, 4 | $2.25 \times 2.00$ | 52.7 | Neptune | 3c84 | 1153+495, 1642+689 |
| 850-7 | 04 | 20100424 | 350 | 6.1 | 7 | 342, 4 | $2.42 \times 2.07$ | -6.1 | Neptune | 3c454.3 | 0958+655, 1642+689 |
| 850-8 | ··· | 20120505 | 380 | 6.0 | 6 | 342, 4 | $1.98 \times 1.84$ | -64.4 | Neptune | 2202+422 | 1153+495, 1642+689 |
| 850-9 | 19 | 20100419 | 410 | 5.8 | 7 | 342, 4 | $2.59 \times 2.07$ | 27.4 | Titan | 3c454.3 | 0958+655, 1642+689 |
| 850-11 | 12 | 20091230 | 380 | 4.8 | 7 | 340, 4 | $2.80 \times 1.96$ | 35.0 | Titan | 3c273 | 0958+655, 1642+689 |
| 850-12 | 15/850.2 | 20100417 | 410 | 4.8 | 7 | 342, 4 | $2.38 \times 2.09$ | 13.9 | Mars | 3c454.3, 3c84 | 0958+655, 1642+689 |
| 850-13 | 21 | 20091231 | 380 | 5.4 | 8 | 340, 4 | $2.27 \times 2.03$ | 13.6 | Titan | 3c273 | 0958+655, 1642+689 |
| 850-15 | 07 | 20100425 | 380 | 6.0 | 7 | 342, 4 | $2.44 \times 1.99$ | 4.7 | Neptune | 3c454.3 | 0958+655, 1642+689 |
| 850-16 | 16 | 20110424 | 340 | 2.6 | 8 | 342, 4 | $2.25 \times 2.00$ | 52.7 | Neptune | 3c454.3 | 1153+495, 1642+689 |
| 850-17 | ··· | 20120501 | 270 | 5.6 | 6 | 342, 4 | $2.48 \times 2.02$ | 63.9 | Titan, Mars | 2202+422 | 1153+495, 1642+689 |

[a] The first number is the frequency center, and the second number is the frequency range for each side band; it is the same number for both side bands.
[b] First track.
[c] Second track.
[d] Each night individually has a different beam size and PA, but since we never use the data separately, we quote here the combined beam size and PA for the two nights.

SMA. We generated continuum data by averaging the spectral channels after doing the passband phase calibration. We used both gain calibrators to derive gain curves. For consistency checks, we compared these results with those obtained by adopting just one calibrator. We did not find any systematic differences. We computed the fluxes using calibrators observed on the same day and under similar conditions (time, hour angle, and elevation). The flux calibration error is typically within $\sim 10\%$ with this method. We exported the calibrated interferometric visibility data to the package MIRIAD for subsequent imaging and analysis. We weighted the visibility data inversely proportional to the system temperature and Fourier transformed them to form images. We also applied the "robust weighting" of Briggs (1995), with a robust parameter of 1.0, to obtain a better balance between beam size and signal-to-noise ratio (S/N). We CLEANed the images around detected sources to approximately 1.5 times the noise level to remove the effects of sidelobes. (The results are not sensitive to choosing a slightly deeper CLEANing level, such as 1.0 times the noise.) We typically achieved rms $\sim 1.2-1.5$ mJy in a night with the old 2 GHz bandwidth and rms $\sim 0.7-0.9$ mJy in a night with the new 4 GHz bandwidth. We corrected the images for the SMA primary beam response. All of the SMA fluxes and flux errors that we quote are primary-beam corrected. We measured source positions and fluxes by fitting the images with point-source models using the MIRIAD IMFIT routine.

## 3. SMA SAMPLE

C13 used their new SCUBA-2 observations of the GOODS-N field (8 mJy sensitivity at $4\sigma$) to test the reliability of the $> 4\sigma$ SCUBA samples of W04 and P05. The SCUBA-2 data rule out at the $> 4\sigma$ level three sources found only in the P05 sample (GN02, GN03, GN08), two sources found only in the W04 sample (GOODS 850-4 and GOODS 850-14), and one source found in both samples (GOODS 850-16 or GN16). We had already observed both GOODS 850-4 and GOODS 850-16 (GN16) with the SMA and had not detected either source. Thus, the SMA and SCUBA-2 observations independently show that these sources are either spurious or are much fainter than the original SCUBA fluxes suggested. Although the SCUBA-2 data did not rule out at the $> 4\sigma$ level GOODS 850-8, we did not detect this source with the SMA, so it also appears to be problematic. We therefore remove the sources GOODS 850-4, GOODS 850-8, GOODS 850-14, and GOODS 850-16 (GN16) from further consideration.

In Table 2, we give the names (Column 1) and J2000 right ascensions (Column 2) and declinations (Column 3), as measured from the SCUBA observations, for all of the unconfirmed sources. We also provide the W04 SCUBA (Column 4), P05 SCUBA (Column 5), C13 SCUBA-2 (Column 6), and SMA (where available; Column 7) fluxes and $1\sigma$ errors.

In Table 3, we give the names (Column 1) of the 12 remaining sources. In cases where we now have multiple SMA detections, we have added an "a", "b", or "c" to the name to distinguish between them. Thus, the sample is actually composed of 16 independent sources rather than 12. *Hereafter, we refer to these 16 sources as our SMA sample.* In Columns 2 and 3, we give the J2000 right ascensions and declinations for each source as measured from the SMA observations. In Column 4, we list the W04 SCUBA fluxes and $1\sigma$ errors; in Column 5, the P05 SCUBA fluxes and $1\sigma$ errors; in Column 6, the C13 SCUBA-2 fluxes and $1\sigma$ errors; and in Column 7, the SMA fluxes and $1\sigma$ errors.

TABLE 2
Unconfirmed SCUBA Sources

| Name GOODS | Name GN/HDF | SCUBA R.A.[a] J2000.0 ($^h$ $^m$ $^s$) | SCUBA Decl.[a] J2000.0 ($^\circ$ $'$ $''$) | W04 SCUBA 850 $\mu$m (mJy) | P05 SCUBA 850 $\mu$m (mJy) | C13 SCUBA-2 850 $\mu$m (mJy) | SMA 860 $\mu$m (mJy) |
|---|---|---|---|---|---|---|---|
| (1) | | (2) | (3) | (4) | (5) | (6) | (7) |
| 850-4 | ··· | 12 36 37.05 | 62 12 08.45 | $8.62 \pm 1.27$ | ··· | -0.4±2.0 | $< 5\,(3\sigma)$ |
| 850-8 | ··· | 12 36 06.30 | 62 12 47.05 | $8.13 \pm 1.40$ | ··· | $3.8 \pm 2.1$ | $< 3.9\,(3\sigma)$ |
| 850-14 | ··· | 12 36 23.45 | 62 13 16.33 | $10.46 \pm 2.32$ | ··· | $2.8 \pm 2.0$ | ··· |
| 850-16 | 16 | 12 37 00.05 | 62 09 15.48 | $12.45 \pm 2.88$ | $9.0 \pm 2.1$ | $0.5 \pm 2.1$ | $< 2\,(3\sigma)$ |
| ··· | 02 | 12 36 07.7 | 62 11 47 | ··· | $16.2 \pm 4.1$ | -1.0±2.0 | ··· |
| ··· | 03 | 12 36 08.9 | 62 12 53 | ··· | $16.8 \pm 4.0$ | $0.7 \pm 2.1$ | ··· |
| ··· | 08 | 12 36 22.2 | 62 12 56 | ··· | $12.5 \pm 2.7$ | -1.4±2.1 | ··· |

[a] Where the source has a GOODS 850 identification, we give the right ascension and declination measurements from W04. Where the source has only a GN identification, we give the right ascension and declination measurements from P05.

TABLE 3
Submillimeter Properties of the SMA Sample

| Name GOODS | Name GN/HDF | SMA R.A. J2000.0 (deg) | SMA Decl. J2000.0 (deg) | W04 SCUBA 850 $\mu$m (mJy) | P05 SCUBA 850 $\mu$m (mJy) | C13 SCUBA-2 850 $\mu$m (mJy) | SMA 860 $\mu$m (mJy) |
|---|---|---|---|---|---|---|---|
| (1) | | (2) | (3) | (4) | (5) | (6) | (7) |
| 850-1 | 14/850.1 | 189.216614 | 62.207165 | $5.1 \pm 0.5$ | $5.9 \pm 0.3$ | $8.0 \pm 2.0$ | $7.8 \pm 1.0$ |
| 850-2 | 09 | 189.092117 | 62.271030 | $10.3 \pm 1.2$ | $8.9 \pm 1.0$ | $6.1 \pm 2.1$ | $9.3 \pm 1.4$ |
| 850-3 | 06 | 189.076370 | 62.264111 | $7.7 \pm 1.0$ | $7.5 \pm 0.9$ | $7.2 \pm 2.1$ | $7.2 \pm 0.7$ |
| 850-5 | 10 | 189.139374 | 62.235752 | $12.9 \pm 2.1$ | $11.3 \pm 1.6$ | $10.5 \pm 2.0$ | $12.0 \pm 1.4$ |
| 850-6 | ··· | 189.378326 | 62.216389 | $13.6 \pm 2.3$ | ··· | $14.9 \pm 2.1$ | $14.9 \pm 0.9$ |
| 850-7 | 04 | 189.067123 | 62.253834 | $6.2 \pm 1.0$ | $5.1 \pm 1.0$ | $7.9 \pm 2.1$ | $3.4 \pm 0.6$ |
| 850-9 | 19 | 189.280045 | 62.235638 | $7.1 \pm 1.2$ | $10.7 \pm 2.7$ | $9.2 \pm 2.0$ | $7.1 \pm 1.4$ |
| 850-11 | 12 | | | $10.8 \pm 2.2$ | $8.6 \pm 1.4$ | $4.3 \pm 2.0$ | |
| a | | 189.192047 | 62.246830 | | | | $4.2 \pm 0.8$ |
| b | | 189.183243 | 62.247417 | | | | $5.3 \pm 1.1$ |
| 850-12 | 15/850.2 | 189.233002 | 62.200531 | $3.3 \pm 0.7$ | $3.7 \pm 0.4$ | $4.2 \pm 2.0$ | $4.5 \pm 0.8$ |
| 850-13 | 21 | | | $7.0 \pm 1.5$ | $5.7 \pm 1.4$ | $2.2 \pm 2.0$ | |
| a | | 189.308472 | 62.199001 | | | | $3.2 \pm 0.9$ |
| b | | 189.309433 | 62.202248 | | | | $4.1 \pm 0.7$ |
| c | | 189.300003 | 62.203415 | | | | $5.3 \pm 0.9$ |
| 850-15 | 07 | | | $8.7 \pm 2.0$ | $8.9 \pm 1.5$ | $0.3 \pm 2.1$ | |
| a | | 189.087921 | 62.285999 | | | | $3.4 \pm 0.6$ |
| b | | 189.088745 | 62.285883 | | | | $3.5 \pm 0.7$ |
| 850-17 | ··· | 189.120160 | 62.179242 | $5.7 \pm 1.4$ | ··· | $-0.1 \pm 2.1$ | $7.7 \pm 0.9$ |

We tested the astrometric accuracy of the SMA observations relative to the GOODS-N 20 cm sample of Owen13. We find that they are in perfect astrometric agreement. The dispersion in the position offsets is $0\farcs5$. The two largest offsets are GOODS 850-12 at $1\farcs3$ and GOODS 850-15a at $0\farcs86$.

We tabulate the multiwavelength properties of the SMA sample in Table 4, and we present the SMA and multiwavelength images in Figure A1 of the Appendix. In Column 1 of Table 4, we give the names of the SMA sources. In Column 2, we give the $3''$ diameter aperture $K_s$ magnitudes corrected to total magnitudes. We measured these at the SMA positions for the isolated galaxies using the $K_s$ image of Wang et al. (2010). We do not provide measurements for GOODS 850-1 (GN14 or HDF850.1), GOODS 850-12 (GN15 or HDF850.2), or GOODS 850-17, where there are nearby bright galaxies.

In Column 3, we give the $2''$ diameter aperture *HST* WFC3 F140W magnitudes corrected to total magnitudes. We measured these at the SMA positions using the F140W images from the archival *HST* slitless WFC3/G141 IR grism survey obtained by B. Weiner (Cycle 17, Proposal 11600). The only exceptions are GOODS 850-1, where we used a $1''$ diameter aperture to minimize contamination from the neighboring galaxies, GOODS 850-15a and 15b, where there is no F140W imaging, and GOODS 850-17, where the flux of the source is too contaminated by the neighboring galaxy.

We searched a $1''$ radius around each SMA position to find optical counterparts in the ACS catalog of Giavalisco et al. (2004). We give the magnitudes of these matches in Columns $4-7$. Note that GOODS 850-2 has a negative flux in the $F140W$ band.

We measured the 20 cm fluxes of the radio sources corresponding to the individual SMA sources in the 39 hr VLA image of Owen13. In Table 5, we give the details of these measurements. In Column 1, we give the names of the SMA sources; in Columns 2 and 3, the SMA J2000 right ascensions and declinations; in Columns 4 and 5, the VLA right ascensions and declinations; in Column 6, for the sources that are not resolved, the upper limits on the sizes of the sources; in Column 7, the peak radio fluxes; in Columns $8-11$, for the sources that are resolved, the total radio fluxes, major axes, minor axes, and position angles for the Gaussian fits.

TABLE 4
MULTIWAVELENGTH PROPERTIES OF THE SMA SAMPLE

| Name | $K_s$ | F140W | F850LP | F775W | F606W | F450W | 20 cm | $0.5-2$ keV | $2-8$ keV | $z_{spec}$ $z_{milli}$[a] |
|---|---|---|---|---|---|---|---|---|---|---|
| GOODS (GN/HDF) | (AB) | (AB) | (AB) | (AB) | (AB) | (AB) | ($\mu$Jy) | ($10^{-16}$ erg cm$^{-2}$ s$^{-1}$) | | |
| (1) | (2) | (3) | (4) | (5) | (6) | (7) | (8) | (9) | (10) | (11) (12) |
| 850-1 (14/850.1) | ··· | 25.77 | ··· | ··· | ··· | ··· | 12.3 (17)[b] | ··· | ··· | 5.183[c] (4.6) |
| 850-2 (09) | 23.92 | -28.19 | ··· | ··· | ··· | ··· | 17.8 | ··· | ··· | ··· 4.3 |
| 850-3 (06) | 21.96 | 23.15 | 26.19 | 27.35 | 28.10 | 29.28 | 161.9 | ··· | ··· | 2.000[d] (1.8) |
| 850-5 (10) | 25.81 | 26.54 | ··· | ··· | ··· | ··· | 32.2 | ··· | ··· | 4.0424[e] (3.9) |
| 850-6 | 22.92 | 24.14 | 25.63 | 25.98 | 25.78 | 25.99 | 117.4 | ··· | ··· | ··· 2.7 |
| 850-7[f] (04) | 22.24 | 23.55 | 25.60 | 25.55 | 38.6 | 27.51 | 38.6 | 1.80 | 7.97 | 2.578[g] (2.3) |
| 850-9[f] (19) | 21.43 | 23.01 | 24.99 | 25.39 | 25.89 | 26.90 | 25.9 | 0.921 | 9.11 | 2.490[h] (3.5) |
| 850-11 (12) | | | | | | | | | | |
| a[f] | 23.25 | 24.23 | 26.02 | 26.21 | 26.73 | 28.44 | 101.8 | -0.339 | -1.38 | ··· 1.7 |
| b | 21.55 | 22.49 | 23.93 | 24.21 | 24.83 | 25.31 | 30.5 | ··· | ··· | 2.095[i] (3.0) |
| 850-12 (15/850.2) | ··· | 23.89 | 24.27 | 24.59 | 24.78 | 25.16 | 19.0 | 1.26 | 2.70 | 2.737[j] (3.3) |
| 850-13 (21) | | | | | | | | | | |
| a | 24.70 | 26.04 | ··· | ··· | ··· | ··· | 21.7 (18)[k] | ··· | ··· | ··· 2.8 |
| b | 21.10 | 22.32 | 23.57 | 23.92 | 24.31 | 24.76 | 23.4 (15)[k] | 2.21 | 5.24 | 3.157[l] (3.0) |
| c | 22.10 | 23.88 | 25.69 | 25.94 | 26.73 | 27.45 | 32.5 | 0.293 | 3.74 | 2.914[m] (2.9) |
| 850-15[f] (07) | | | | | | | | | | |
| a | 21.77 | ··· | 23.57 | 23.92 | 24.34 | 24.67 | 43.2 | ··· | ··· | 1.992[n] (2.2) |
| b | 21.68 | ··· | 26.81 | 27.83 | 28.68 | 28.41 | 146.9 | ··· | ··· | ··· 1.4 |
| 850-17[f] | ··· | ··· | ··· | ··· | ··· | ··· | 48.5[o] | ··· | ··· | ··· 2.8 |

[a] Where a spectroscopic redshift already exists for the source, we put the millimetric redshift in parentheses.
[b] The quantity in brackets is the previous measurement from Cowie et al. (2009).
[c] The IRAM PdBI CO[5-4], CO[6-5], and [CII] redshift of $z = 5.183$ is from Walter et al. (2012).
[d] The Pope et al. (2008) *Spitzer* IRS redshift of $z = 2.00 \pm 0.03$ is inconsistent with the optical redshift of $z = 1.865$ from Chapman et al. (2005). Bothwell et al. (2010) found an IRAM PdBI CO[4-3] redshift of $z = 1.999 \pm 0.001$ for the source, which they called HDF 132.
[e] The IRAM PdBI CO[4-3] redshift of $z = 4.0424$ is from Daddi et al. (2009a).
[f] These sources have close pairs of radio sources.
[g] The brighter radio source has an optical redshift of $z = 2.578$ from Chapman et al. (2005). The fainter radio source lacks an optical counterpart. The counterpart to the brighter radio source, which is at the position of the SMA source, is a chain-like object with three components. The magnitudes in the table correspond to the reddest component in this structure, which is closest to the SMA and VLA positions. If the components are not physically related, then the redshift may not correspond to the submillimeter galaxy.
[h] The two equally bright radio sources have optical redshifts of $z = 2.484$ from Chapman et al. (2005). The NIR redshift of $z = 2.490$ is from Swinbank et al. (2004). The *Spitzer* IRS redshift of $z = 2.48 \pm 0.03$ is from Pope et al. (2008).
[i] The optical redshift of $z = 2.095$ is from Reddy et al. (2006).
[j] The optical redshift of $z = 2.737$ is from Barger et al. (2008).
[k] The quantities in brackets are the previous measurements from Wang et al. (2011).
[l] The optical redshift of $z = 3.157$ is from Barger et al. (2008).
[m] The optical redshift of $z = 2.914$ is from Chapman et al. (2005).
[n] The optical redshift of $z = 1.99$ for the brighter optical but fainter radio source of the GOODS 850-15a/850-15b pair is from Chapman et al. (2004). The NIR redshift of $z = 1.992$ for the same source is from Swinbank et al. (2004).
[o] The neighboring radio/X-ray source previously identified as the correct counterpart to this submillimeter galaxy has an optical redshift of $z = 1.013$ from Barger et al. (2008). We now know the other radio source is the correct counterpart to this submillimeter galaxy.

TABLE 5
Radio Measurements

| Name | | SMA R.A. | SMA Decl. | VLA R.A. | VLA Decl. | Upper | Peak Radio | Total Radio | Major | Minor | P.A. |
|---|---|---|---|---|---|---|---|---|---|---|---|
| GOODS | GN/HDF | J2000.0 | J2000.0 | J2000.0 | J2000.0 | Limit | Flux | Flux | Axis | Axis | |
| | | ($^h$ $^m$ $^s$) | ($^\circ$ $'$ $''$) | ($^h$ $^m$ $^s$) | ($^\circ$ $'$ $''$) | ($''$) | ($\mu$Jy/beam) | ($\mu$Jy) | ($''$) | ($''$) | (deg) |
| (1) | | (2) | (3) | (4) | (5) | (6) | (7) | (8) | (9) | (10) | (11) |
| 850-1 | 14/850.1 | 12 36 51.98 | 62 12 25.8 | 12 36 52.04 | 62 12 25.9 | $< 1.5$ | $12.3 \pm 2.4$ | ··· | ··· | ··· | ··· |
| 850-2 | 09 | 12 36 22.11 | 62 16 15.7 | 12 36 22.11 | 62 16 15.9 | $< 1.6$ | $17.8 \pm 2.5$ | ··· | ··· | ··· | ··· |
| 850-3 | 06 | 12 36 18.33 | 62 15 50.8 | 12 36 18.35 | 62 15 50.6 | ··· | $155.0 \pm 2.7$ | $161.9 \pm 4.8$ | 0.5 | 0.4 | $129 \pm 21$ |
| 850-5 | 10 | 12 36 33.45 | 62 14 08.7 | 12 36 33.42 | 62 14 08.5 | ··· | $20.6 \pm 2.3$ | $32.2 \pm 5.5$ | 1.9 | 0 | $72 \pm 8$ |
| 850-6 | ··· | 12 37 30.80 | 62 12 59.0 | 12 37 30.81 | 62 12 58.8 | $< 0.6$ | $117.4 \pm 2.7$ | ··· | ··· | ··· | ··· |
| 850-7 | 04 | 12 36 16.11 | 62 15 13.8 | 12 36 16.11 | 62 15 13.7 | $< 1.1$ | $38.6 \pm 2.6$ | ··· | ··· | ··· | ··· |
| comp | ··· | ··· | ··· | 12 36 15.84 | 62 15 15.6 | $< 0.4$ | $28.7 \pm 2.6$ | ··· | ··· | ··· | ··· |
| 850-9 | 19 | 12 37 07.21 | 62 14 08.3 | 12 36 16.11 | 62 15 13.7 | $< 1.0$ | $25.9 \pm 2.5$ | ··· | ··· | ··· | ··· |
| comp | ··· | ··· | ··· | 12 37 07.60 | 62 14 09.6 | $< 1.0$ | $28.3 \pm 2.5$ | ··· | ··· | ··· | ··· |
| 850-11 | 12 | | | | | | | | | | |
| a | | 12 36 46.09 | 62 14 48.6 | 12 36 46.08 | 62 14 48.6 | $< 0.7$ | $101.8 \pm 2.4$ | ··· | ··· | ··· | ··· |
| comp | ··· | ··· | ··· | 12 36 46.81 | 62 14 45.5 | ··· | $42.4 \pm 2.3$ | $68.9 \pm 5.7$ | 2.1 | 0 | $133 \pm 5$ |
| b | | 12 36 43.98 | 62 14 50.7 | 12 36 44.03 | 62 14 50.6 | $< 0.6$ | $30.5 \pm 2.4$ | ··· | ··· | ··· | ··· |
| 850-12 | 15/850.2 | 12 36 55.92 | 62 12 01.9 | 12 36 55.80 | 62 12 00.9 | ··· | $13.1 \pm 2.4$ | $19.0 \pm 5.4$ | 1.6 | 0.3 | $34 \pm 12$ |
| 850-13 | 21 | | | | | | | | | | |
| a | | 12 37 14.03 | 62 11 56.40 | 12 37 14.05 | 62 11 56.6 | $< 1.1$ | $21.7 \pm 2.5$ | ··· | ··· | ··· | ··· |
| b | | 12 37 14.26 | 62 12 08.1 | 12 37 14.29 | 62 12 08.5 | $< 1.3$ | $23.4 \pm 2.5$ | ··· | ··· | ··· | ··· |
| c | | 12 37 12.00 | 62 12 12.3 | 12 37 12.06 | 62 12 11.9 | $< 0.7$ | $32.5 \pm 2.4$ | ··· | ··· | ··· | ··· |
| 850-15 | 07 | | | | | | | | | | |
| a | | 12 36 21.10 | 62 17 09.6 | 12 36 20.98 | 62 17 09.8 | $< 1.0$ | $43.2 \pm 2.6$ | ··· | ··· | ··· | ··· |
| b | | 12 36 21.30 | 62 17 09.2 | 12 36 21.28 | 62 17 08.4 | $< 0.6$ | $146.9 \pm 2.6$ | ··· | ··· | ··· | ··· |
| 850-17[a] | ··· | 12 36 28.84 | 62 10 45.3 | 12 36 28.90 | 62 10 45.3 | ··· | $35.0 \pm 3.9$ | $48.5 \pm 9.4$ | 0.7 | 0.4 | $73 \pm 40$ |
| comp | ··· | ··· | ··· | 12 36 29.16 | 62 10 46.0 | ··· | $36.5 \pm 3.9$ | $48.1 \pm 8.2$ | 1.0 | 0 | $30 \pm 12$ |

[a] For this source, we use the Gaussian fit from the higher resolution ($\sim 1''$) image, which separates the radio pair better. The noise in slightly higher in this image.

Six of the SMA sources (GOODS 850-7 (GN04), GOODS 850-9 (GN19), GOODS 850-11a (GN12), GOODS 850-15a and GOODS 850-15b (GN07), GOODS 850-17) constitute one-half (or, in the case of GOODS 850-15a and GOODS 850-15b, a whole) of a radio pair having separations between the two radio sources $< 5''$. Thus, in Table 5, for each of these pairs (except GOODS 850-15a and GOODS 850-15b, which are both already in the table), we give the radio measurements of the second radio source below that of the first radio source and label it "comp". We note that because GOODS 850-17 is such a close radio pair, we decided to use the Gaussian fit from the higher resolution ($\sim 1''$) radio image, which separates the radio pair better. The noise is slightly higher in this image.

Returning to Table 4, for the resolved radio sources, we quote the total radio flux density in Column 8. Otherwise, we quote the peak radio flux density. For the radio sources that are one of a pair, we only quote the radio flux density corresponding to the SMA source. The radio flux density for GOODS 850-17 is that measured from the higher resolution image.

We searched a $3''$ radius around each SMA position to find X-ray counterparts in the 2 Ms *Chandra* catalog of Alexander et al. (2003b). All of the X-ray counterparts are within $1\farcs5$ of the SMA positions except GOODS 850-17. For GOODS 850-17 the X-ray source is at the position of the second radio source in the pair and not at the position of the SMA source, so we eliminated this match. We give the soft and hard X-ray fluxes of the remaining matches in Columns 9 and 10, respectively.

We searched the literature for spectroscopic redshifts, which we summarize in Column 11. We give the origins of the redshifts in the table notes. Finally, in Column 12, we give the millimetric redshifts that we estimate in Section 4.3.2. Where a spectroscopic redshift already exists for the source, we put the millimetric redshift in parentheses.

## 4. RESULTS

### 4.1. *Multiplicity*

The first conclusion that we draw from our SMA observations is that the number of bright SMGs in the GOODS-N is significantly overestimated in all of the existing SCUBA catalogs. First, as we noted in Section 3, there are a number of sources in both the W04 and P05 catalogs that are not detected in the SMA and SCUBA-2 observations. Second, there are three SMGs (GOODS 850-11 or GN12, GOODS 850-13 or GN21, and GOODS 850-15 or GN07) that are composed of multiple fainter objects blended in the single-dish observations to form a single, apparently more luminous object.

In Figure 1, we show the fluxes from our SMA observations versus the fluxes from the original SCUBA observations (W04). For the single SMA sources (red squares), the fluxes are in good agreement. For the multiple SMA sources composing one SCUBA source, in each case, the individual SMA sources have lower fluxes than the SCUBA source, because the latter's flux is a blend of all the SMA source fluxes. Thus, in Figure 1(a), we show the multiple sources (blue diamonds) as separate SMA sources plotted at a common SCUBA 850 $\mu$m flux. However, in Figure 1(b), we plot the multiple sources (blue diamonds) after combining their SMA fluxes. For sources with smaller separations (i.e., the two double sources), these combined SMA fluxes match the SCUBA fluxes well. However, for the triple source, where the separations between the sources approach the SCUBA FWHM, the combined SMA flux is larger than the SCUBA flux (not shown; see below), which measures only the portion within the beam. Wang et al. (2011) note that GOODS 850-13a, 13b, and 13c actually combine to match two SCUBA sources (GOODS 850-13 and GOODS 850-23) in the W04 catalog. We therefore plot the combined SCUBA fluxes of GOODS 850-13 and GOODS 850-23 in Figure 1(b). With this adjustment, the total SMA flux of the triple source also agrees well with the SCUBA flux.

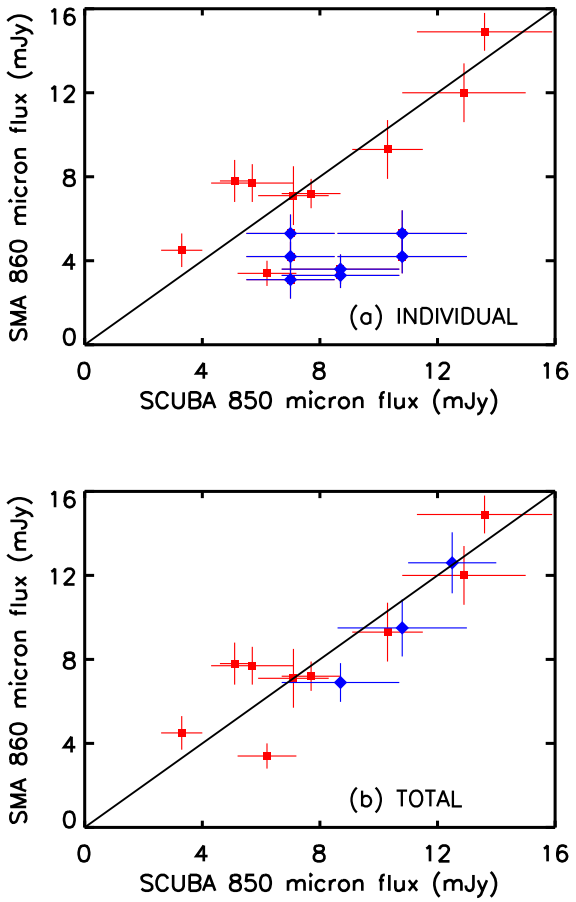



FIG. 1.— (a) SMA 860 $\mu$m flux vs. SCUBA 850 $\mu$m flux for the SMA sample in the GOODS-N. SCUBA sources found to be single in the SMA images are shown with red squares with $1\sigma$ uncertainties. SCUBA sources found to be multiples in the SMA images are shown with blue diamonds with $1\sigma$ uncertainites. In these cases the individual SMA fluxes are lower than the SCUBA flux, which is the blended flux of all the individual sources. (b) Total SMA 860 $\mu$m flux from the combined individual sources vs. SCUBA 850 $\mu$m flux. The single sources are again shown as red squares, and the multiple sources as blue diamonds. Here we have combined the SCUBA fluxes of GOODS 850-13 and GOODS 850-23 (W04) to compare with the combined SMA fluxes of GOODS 850-13a, 13b, and 13c (see text for details).

For the five sources with 850 $\mu$m SCUBA fluxes above 8 mJy in the SMA sample (see Column 4 of Table 3), the average sensitivity of the SMA observations is such

that we could differentiate cases where two comparable sources were contributing to the SCUBA flux. We find that three of the five sources are single sources, where the SMA flux matches the SCUBA flux, while the remaining two sources are multiples. Above an 850 $\mu$m flux of 7 mJy, three of the eight sources are found to be multiples. These results suggest that 37.5% of bright SMGs are actually blends, though with such small numbers, the uncertainties in the precise fraction are large (the $\pm1\sigma$ range is 17% to 74%).

Smolčić et al. (2012) performed interferometric continuum followup with the IRAM PdBI at 1.3 mm of a sample of 28 SMGs detected in the COSMOS field at 870 $\mu$m with LABOCA. Because they did not require the LABOCA SMGs to be detected at high significance ($> 4\sigma$), and because they had a wavelength mismatch between the discovery observations and their followup observations, it is difficult to make precise comparisons. However, they discovered that 6 of the 19 LABOCA sources that they detected in their 1.3 mm maps broke up into multiple sources. [Due to the multiples, they note that, in total, this means they detected 26 SMGs, but the significance of the detections ranges from $4.5\sigma$ (9 sources), to $4-4.5\sigma$ (7 sources), down to $3-4\sigma$ (10 sources).] When they added in the 8 LABOCA sources that had previously been observed and detected with millimeter interferometers (CARMA, SMA, PdBI), the fraction became 6 multiples out of 27 detections (22%±9%). Given the heterogeneous nature of the sample, the percentages are quite uncertain, but it is reassuring that they are broadly consistent with our results.

A comparison with Magnelli et al. (2012) illustrates some of the problems that can arise from not having high-resolution imaging data. Magnelli et al. (2012) performed a detailed analysis of a sample of 61 SMGs (both lensed and unlensed) detected at a range of significances in a number of fields, including the GOODS-N, at either submillimeter or millimeter wavelengths using a variety of ground-based telescopes and instruments. In their Section 3.6, Magnelli et al. state that GOODS 850-7 (GN04) has two optical counterparts and that the IRAC photometry of the two counterparts is consistent with them being at the same redshift. They therefore assume that it is an interacting pair and derive the dust properties of GOODS 850-7 (GN04) by adding the MIR, FIR, and radio[2] fluxes of the two "counterparts" together. However, our SMA observations clearly show that the submillimeter emission arises from only one of the two IRAC sources (see Figure A1).

In summary, a uniformly selected, high-significance, and well-understood SMG sample with high-resolution imaging data at the wavelength of detection is very important. This becomes particularly essential when we try to test whether high-redshift sources obey local relations, such as the FIR-radio correlation. Otherwise, the scatter in the relations may easily be overestimated and systematic effects introduced.

[2] Although the radio fluxes given in Table 3 of Magnelli et al. (2012) are said to be from the Morrison et al. (2010) catalog, this does not appear to be the case. For example, for GOODS 850-7 (GN04), Magnelli et al. list a radio flux density of $89.5\pm6.3$ $\mu$Jy, but the flux density given in the Morrison et al. catalog for this source is 34 $\mu$Jy.

### 4.2. *Radio Properties*

As we discussed in the introduction, often SMGs are found to have multiple candidate radio counterparts. However, SMA observations have shown that not all of these candidate radio counterparts produce submillimeter emission (e.g., Younger et al. 2007, 2008, 2009).

For example, Ivison et al. (2007) found that the fraction of radio-identified SMGs with multiple candidate radio counterparts in the SCUBA HAlf Degree Extragalactic Survey (SHADES) was $18.5\pm5.3\%$ (12/65), of which $15.4\pm4.9\%$ (10/65) had separations below $6''$. However, Hatsukade et al. (2010) found that their measured SMA flux ($S_{880\ \mu\mathrm{m}} = 6.9\pm1.2$ mJy) for the SHADES source SXDF 850.6 ($S_{850\ \mu\mathrm{m}} = 8.15\pm2.2$ mJy from SCUBA; Coppin et al. 2006) came from only one of the three possible radio counterparts identified by Ivison et al. (2007), even though all three radio sources have corresponding MIPS 24 $\mu$m sources (Clements et al. 2008).

In Figure 2, we show 20 cm contours from the GOODS-N VLA image of Owen13 overlaid on *HST* F140W images [$K_s$ images for GOODS 850-15a, 15b (GN07), where there is no F140W coverage]. Each thumbnail in the figure is centered on the SMA position. All of the sources in our SMA sample are detected in the radio image. There are five radio pairs with separations between the sources of $< 5''$ (GOODS 850-7 (GN04), GOODS 850-9 (GN19), GOODS 850-11a (GN12), GOODS 850-15a, 15b (GN07), GOODS 850-17). However, only for GOODS 850-15a, 15b (GN07) does a submillimeter counterpart exist for both radio sources in the pair.

In Figure 3, we plot 20 cm flux (Column 8 of Table 4) versus SMA flux (Column 7 of Table 3) for the sources in the SMA sample. There is no obvious dependence of the 20 cm flux on the 860 $\mu$m flux. Because all of the SMA sources are detected in the radio at $> 5\sigma$, we can calculate the radio luminosities, subject to the assumptions about the radio spectral index that we discuss in Section 5.2, once we have the redshifts for the sources.

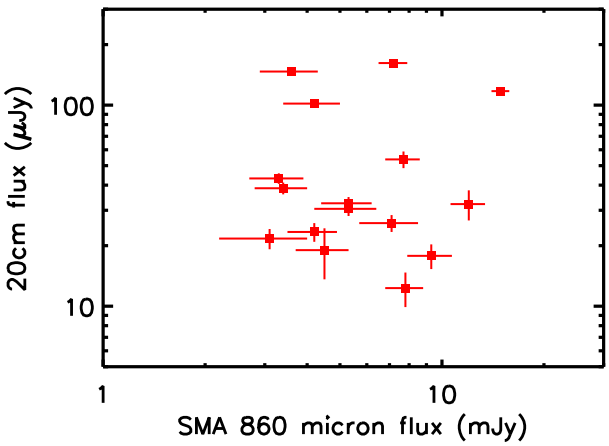



FIG. 3.— 20 cm flux vs. 860 $\mu$m flux with $\pm1\sigma$ uncertainties for the SMA sample.

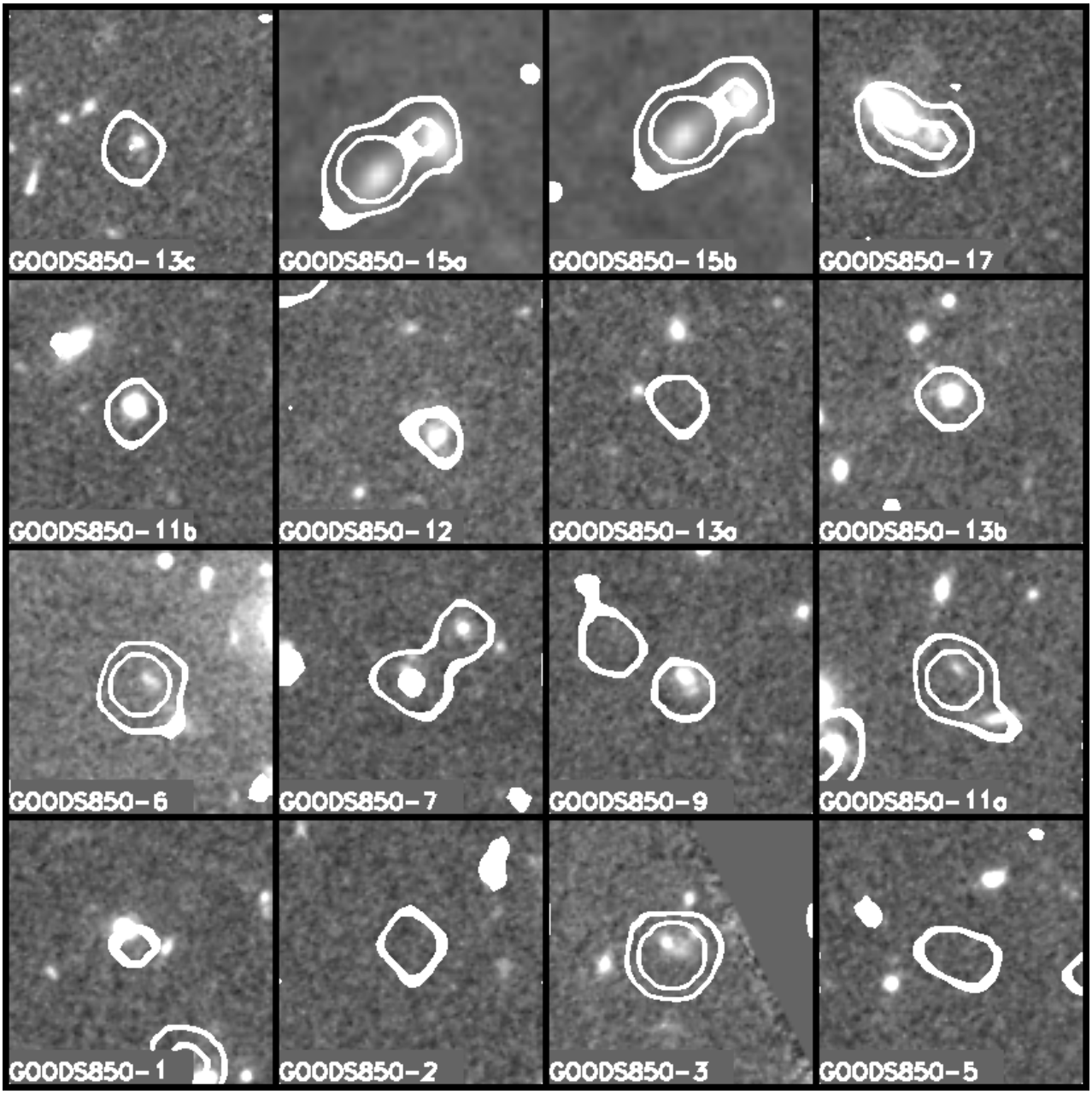



FIG. 2.— 20 cm contours overlaid on the *HST* F140W images centered on the SMA positions of the SMA sample. The panels are $10''$ on a side. The F140W images were obtained from the *HST* archive and are 811 s exposures. The 20 cm image is from Owen13. GOODS 850-15a, 15b are off the GOODS-N area observed in F140W, so for them we show the $K_s$ image from Wang et al. (2010). The depth of the $K_s$-band image is comparable, but the resolution is poorer. The lowest contour is chosen to be well above the noise level in the 20 cm image. The second contour is a factor of two higher in surface brightness to show the position of peaks in the radio. Because of smoothing, the radio contours are not a good representation of the 20 cm image quality. The properties of the sources that are spatially extended are given in Table 5.

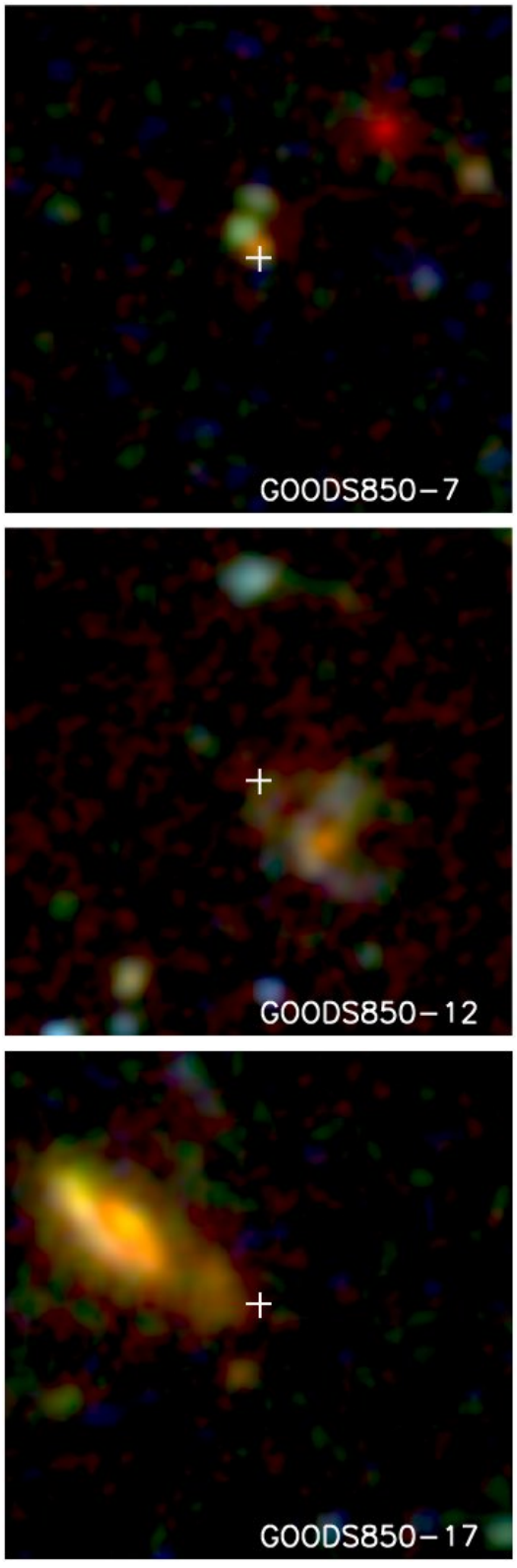



FIG. 4.— F450W ($B$), F775W ($I$) and F140W ($H$) three-color images of three SMGs in the SMA sample for which the identifications of the counterparts at other wavelengths are not straightforward. (Top) For GOODS 850-7 (GN04), the counterpart is a chain-like galaxy consisting of three components with very varied colors. (Center) For GOODS 850-12 (GN15/HDF 850.2), the submillimeter emission lies near an apparently merging system, which is an X-ray source. (Bottom) For GOODS 850-17, the submillimeter emission lies off the edge of a bright galaxy, which is both an X-ray and radio source. In this case, we assume the submillimeter emission is not physically related to the bright galaxy, and hence we do not assign the redshift of the bright galaxy to the SMG.

### 4.3. *Redshifts*

#### 4.3.1. *Spectroscopic*

The accurate submillimeter positions from the SMA allow us to make a more critical assessment of the existing spectroscopic redshift identifications. We summarize the redshift information from the literature in Table 4, where we give both the redshift (Column 11) and the reference (table notes). Unfortunately, even with our accurate positions, there can still be uncertanties in assigning the redshifts.

In Figure 4, we show the three most difficult cases from our SMA sample using three-color ($BIH$) images marked with white crosses at the positions of the submillimeter emission. In the top panel, we show the region around GOODS 850-7 (GN04). This source appears to be a chain galaxy (Cowie et al. 1995), consisting of three knots with very varied colors. The spectroscopic redshift of $z = 2.578$ from Chapman et al. (2005) relates to the upper bluer regions, but the knot corresponding to the submillimeter emission is much redder. The magnitudes in the table correspond to this redder component. Given the configuration, we accept the redshift as applying to the SMG, but we caution that it could still be a chance projection.

In the center panel, we show the region around GOODS 850-12 (GN15/HDF 850.2). The submillimeter emission arises from a location near an X-ray source that has a redshift of $z = 2.737$ from Barger et al. (2008). The X-ray source, which appears to be part of a merging system with outlying debris, was tentatively identified by P06 as the counterpart to the SMG. We feel it is likely that the submillimeter emission is associated with the merging system and therefore accept the redshift as applying to the SMG, but again we caution that it could still be a chance projection.

In the bottom panel, we show the region around GOODS 850-17. Here the submillimeter emission lies off the edge of a much brighter galaxy. The bright galaxy is an X-ray and radio source with a redshift of $z = 1.013$ from Barger et al. (2008). Although it is possible that this is a merging system, in which case the redshift would also apply to the SMG, it is also possible that the SMG is a chance projection, possibly amplified by gravitational lensing due to the larger galaxy. Given its $2.3''$ offset from the radio and X-ray source, we do not accept this redshift identification for the SMG. (Note that Bothwell et al. (2012) also did not detect GOODS 850-17 with the IRAM PdBI in CO[2-1] at this redshift.)

With the above assignments for these three difficult cases, we have spectroscopic redshifts for 10 of the 16 SMGs (8 optical/IR and 2 CO) with values ranging from $z = 2 - 5.2$.

#### 4.3.2. *Millimetric*

As we discussed in Section 4.2, with our accurate SMA positions, we can unambiguously determine the radio counterparts to the SMGs, and with the new ultradeep 20 cm data of Owen13, we find counterparts to all of the SMA sources above the $5\sigma$ threshold of 12.5 $\mu$Jy (see Figure 2 and Table 5). In combination with the spectroscopic redshifts, this allows us to test previous efforts to

estimate redshifts for the SMGs using 20 cm to 860 $\mu$m flux ratios in a precise way that was not previously possible. (Following Barger et al. 2000, we refer to such estimates as millimetric redshifts.)

In Figure 5, we plot the radio to submillimeter flux ratios versus $1+z$ using spectroscopic redshifts, where available, for the SMGs in the SMA sample (black squares). For the SMGs in the sample without spectroscopic redshifts, we plot them at a nominal redshift of $z = 0.2$ (blue diamonds). We distinguish sources that contain AGNs based on their X-ray fluxes with red boxes, but these are expected to follow the same relation as the non-AGNs, since both star-forming galaxies and radio-quiet AGNs obey the same FIR-radio correlation (Condon 1992). We find that the SMGs with spectroscopic redshifts can be fit by a power law (black line). We also show on the plot the Arp 220-based model of Barger et al. (2000) (blue line) and the M82-based model of Carilli & Yun (1999) (red dashed line). The Barger et al. (2000) model agrees reasonably well with the power law fit over the observed spectroscopic redshift range. We therefore adopt this relation (Equation 5 of Barger et al. 2000) to measure millimetric redshifts for the SMGs in our SMA sample.

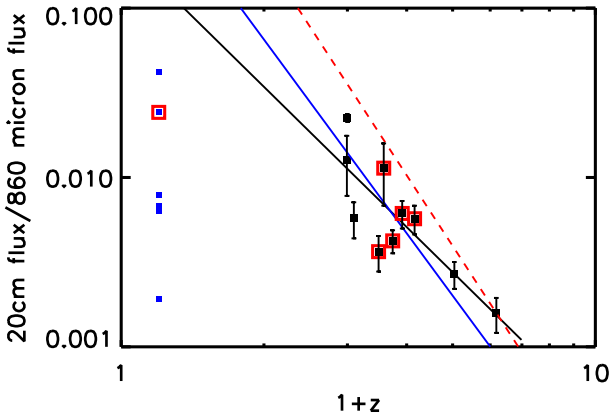



FIG. 5.— 20 cm to 860 $\mu$m flux ratio vs. 1+z for the SMGs in the SMA sample with spectroscopic redshifts (black squares). The SMGs in the sample without spectroscopic redshifts (blue squares) are shown at a nominal redshift of $z = 0.2$. SMGs with X-ray detections are marked with red boxes. The error bars are $\pm 1\sigma$. The black line shows a power law fit to the data. The blue line shows the Arp 220-based model of Barger et al. (2000). The red dashed line shows the M82-based model of Carilli & Yun (1999).

In Figure 6, we plot the millimetric redshifts versus the spectroscopic redshifts, where available, for the SMGs in the SMA sample (black squares). For the SMGs in the sample without spectroscopic redshifts, we plot them at their millimetric redshifts in both axes (blue diamonds). We find that the millimetric redshifts generally reproduce the spectroscopic redshifts with a maximum multiplicative uncertainty of about 1.4. We show the redshift distributions in histogram form at the bottom of the plot. We use the blue histogram to show the redshift distribution of the full sample using the combined spectroscopic and millimetric redshifts, while we use the black filled histogram to show the redshift distribution of the spectroscopically identified sources only. The spectroscopic redshifts range from $z = 2 - 5.2$, while the millimetric redshifts of the remaining sources range from $z = 1.3 - 4.3$. Within the systematic uncertainties, the two redshift ranges could be nearly identical.

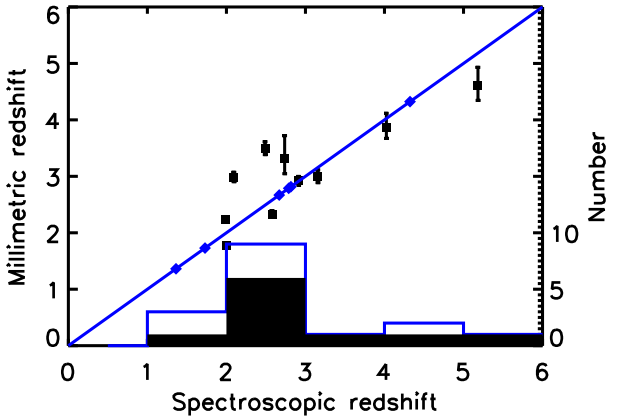



FIG. 6.— Millimetric redshift estimated from the 20 cm to 860 $\mu$m flux ratio using the Barger et al. (2000) Arp 220-based model vs. spectroscopic redshift. The SMGs in the SMA sample with spectroscopic redshifts are denoted by black squares, while those without spectroscopic redshifts are denoted by blue diamonds and are plotted at their millimetric redshifts in both axes. The blue histogram shows the redshift distribution of the full sample using the combined spectroscopic and millimetric redshifts, while the black filled histogram shows the redshift distribution of the spectroscopically identified sources only.

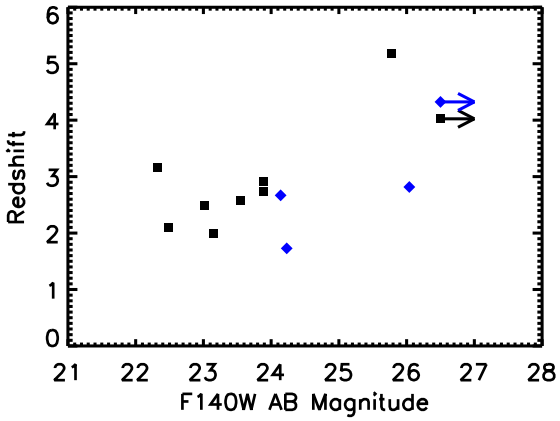



FIG. 7.— Redshift vs. F140W AB magnitude for the SMGs in the SMA sample with measured F140W magnitudes. This excludes GOODS 850-15a, b (GN07), for which there is no F140W coverage, and GOODS-17, for which there is too much contamination from the neighboring source to make a measurement. The SMGs with spectroscopic redshifts are denoted by black squares, while those with only millimetric redshifts are denoted by blue diamonds. The right-pointing arrows show the $2\sigma$ limit of the F140W image of 26.5.

### 4.4. *Optical/NIR Properties*

Very high-redshift SMGs are often very faint in the optical/NIR (e.g., Wang et al. 2009; Cowie et al. 2009). Thus, it is worth investigating with our SMA sample whether there is a particular NIR magnitude limit that separates sources at lower redshifts from those at higher redshifts.

In Figure 7, we plot redshift versus F140W AB mag-

nitude for the SMGs in the SMA sample with measured F140W magnitudes. The black squares denote sources with spectroscopic redshifts, while the blue diamonds denote sources with only millimetric redshifts. Two of the SMGs have magnitudes fainter than the $1\sigma$ limit of the F140W image of 26.5 (arrows). There exists about a 1 mag gap in the plot between the lower redshift sources ($z < 3.5$) and the mostly high-redshift sources, but the total number of sources is very small.

## 5. CLEAN SMA SAMPLE

The primary goal of this work is to understand the properties of a highly significant and complete 850 $\mu$m selected sample of SMGs for which we know accurate fluxes and positions from the SMA. We do not require spectroscopic redshifts, but we use them wherever available, since they help with determining accurate temperatures and spectral energy distributions (SEDs). Otherwise, we estimate millimetric redshifts, which we can do straightforwardly, since all of the sources in our SMA sample are detected in the new ultradeep 20 cm image of Owen13.

Using the measurements in the FIR, submillimeter, and millimeter, we now want to compare the shapes of the thermal spectra of our SMGs with those of local ultraluminous infrared galaxies (ULIRGs). In order to do this properly, however, we need to avoid SMGs that are composed of multiple sources, each of which may be at a different redshift, as well as SMGs that are blended with neighboring galaxies at FIR wavelengths due to the large beam FWHM sizes of *Herschel* ($\sim 17''$ at 250 $\mu$m, $\sim 24''$ at 350 $\mu$m, and $\sim 35''$ at 500 $\mu$m; see bottom panels of Figure A1 in the Appendix). In all of these cases, it would be impossible to disentangle the different dust temperatures. Finally, the SMGs cannot be too faint in the FIR to have *Herschel* detections, or else we would not be able to map the peak of the dust spectrum.

Thus, for this portion of our analysis, we need to remove from our SMA sample the multiple sources (GOODS 850-11a, b (GN12), GOODS 850-13a, b, c (GN21), and GOODS 850-15a, b (GN07)); the sources that are too close to a neighboring galaxy for accurate *Herschel* FIR measurements (GOODS 850-2 (GN09) and GOODS 850-17); and the sources that do not have *Herschel* detections (GOODS 850-1 (GN14/HDF850.1) and GOODS 850-12 (GN15/HDF850.2)). This leaves us with a clean sample of 5 sources, 4 of which have spectroscopic redshifts and 1 (GOODS 850-6) of which has only a millimetric redshift. Hereafter, we refer to this as our clean SMA sample.

### 5.1. *Spectral Energy Distributions*

In Table 6, we list, where available, the MIR through millimeter flux measurements for each of the 5 SMGs in our clean SMA sample, providing the corresponding references for the flux measurements in the table notes. We show these measurements in Figures 8(a) and 8(b) as different colored symbols (diamonds for the FIR, submillimeter, and millimeter data, and squares for the MIR and radio data) for each source. Due to the dense clustering of the data points, we only show error bars on the radio data to maintain the clarity of the plots. However, the errors on the radio data are comparable to the symbol size for most of the galaxies. In Figure 8(b), we also include the Arp 220 data points (open triangles) from Klaas et al. (1997). From this figure we can see that the Arp 220 MIR data points drop below the SMG MIR data points, which are measured at slightly shorter rest-frame wavelengths. This suggests that the PAH emission strength is stronger at higher redshifts, as also noted by Magnelli et al. (2012).

At longer wavelengths, the dust emission from local luminous infrared galaxies is well described (e.g., see Klaas et al. 1997) by optically thin, single temperature modified blackbodies, $S_\nu \propto \nu^\beta B_\nu(T)$, where $\beta$ is the emissivity parameter and is determined empirically. More complex fits that include MIR data are also often used (e.g., Casey 2012 and references therein), but we have no data between rest-frame wavelengths of 8 and 40 $\mu$m, so we stay with the simpler model.

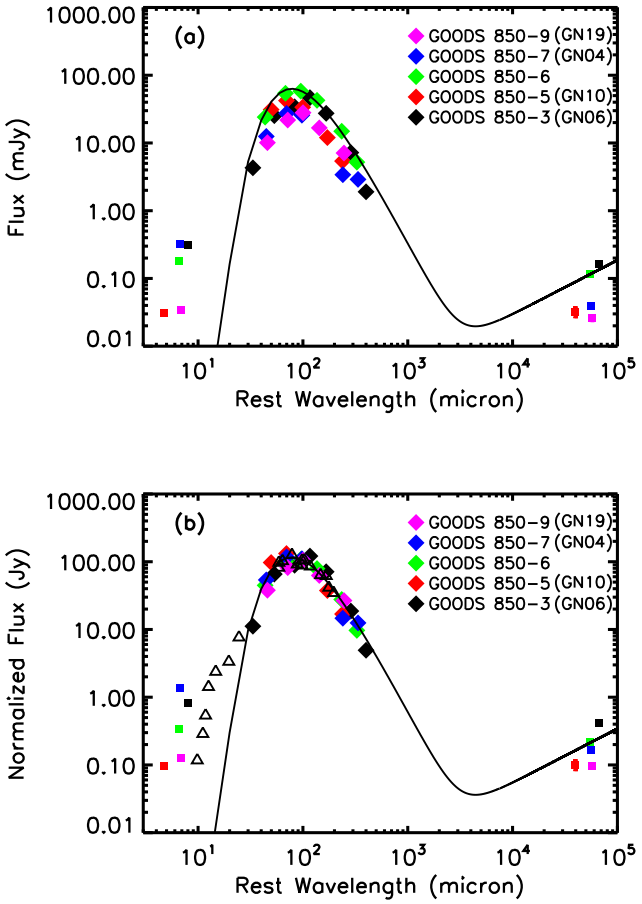



FIG. 8.— The SEDs for the 5 SMGs in our clean SMA sample (colored diamonds for the FIR, submillimeter, and millimeter data, and squares for the MIR and radio data). For clarity, error bars are only shown for the radio data. The radio measurements are given in Table 5, and the MIR through millimeter measurements are given in Table 6. In each panel the black curve shows a modified blackbody fit to the Arp 220 data points of Klaas et al. (1997) with $\beta = 1$ and a dust temperature of $T_d = 47$ K. (a) Here the modified blackbody is normalized to GOODS 850-6, the one source with only a millimetric redshift. (b) Here the modified blackbody is shown as the original fit to the Arp 220 data points of Klaas et al. (1997; open triangles), and the SMGs are normalized to have the same value as Arp 220 at rest-frame 100 $\mu$m, the peak of the distribution where the SEDs are relatively flat.

At higher redshifts, Barger et al. (2000) used the Klaas

TABLE 6
MIR/FIR/Submillimeter/Millimeter Fluxes

| Name | | 24 $\mu$m | 100 $\mu$m | 160 $\mu$m | 250 $\mu$m | 350 $\mu$m | 500 $\mu$m | 860 $\mu$m | 1100 $\mu$m |
|---|---|---|---|---|---|---|---|---|---|
| GOODS | GN/HDF | ($\mu$Jy) | (mJy) | (mJy) | (mJy) | (mJy) | (mJy) | (mJy) | (mJy) |
| (1) | | (2) | (3) | (4) | (5) | (6) | (7) | (8) | (9) |
| 850-3[a] | 06 | $314.5 \pm 4.1$ | $4.3 \pm 1.0$ | $25.3 \pm 2.0$ | $34.2 \pm 3.1$ | $46.7 \pm 4.0$ | $27.4 \pm 4.0$ | $7.2 \pm 0.7$ | $1.9 \pm 1.4$ |
| 850-5[b] | 10 | ··· | $30.7 \pm 6.0$ | ··· | $31.1 \pm 3.1$ | $42.2 \pm 4.0$ | $33.7 \pm 4.0$ | $12.0 \pm 1.4$ | $5.4 \pm 1.1$ |
| 850-6[c] | ··· | $184.0 \pm 4.2$ | ··· | $24.1 \pm 1.9$ | $54.1 \pm 3.1$ | $58.2 \pm 4.0$ | $42.6 \pm 4.0$ | $14.9 \pm 0.9$ | $4.1 \pm 1.1$ |
| 850-7[d] | 04 | $322.5 \pm 4.5$ | ··· | $12.5 \pm 1.9$ | $27.3 \pm 3.1$ | $25.7 \pm 4.0$ | ··· | $3.4 \pm 0.6$ | $2.9 \pm 1.1$ |
| 850-9[e] | 19 | $33.9 \pm 5.4$ | ··· | $10.1 \pm 1.6$ | $21.8 \pm 3.1$ | $28.0 \pm 4.0$ | $16.7 \pm 3.9$ | $7.1 \pm 1.4$ | ··· |

[a] The 24 $\mu$m flux is from Magnelli et al. (2011). The separation between the 24 $\mu$m source position and the SMA position is $0.45''$. The 100 $\mu$m, 160 $\mu$m, 250 $\mu$m, 350 $\mu$m, and 500 $\mu$m fluxes are from Magnelli et al. (2012). The 860 $\mu$m flux is from this paper. The 1100 $\mu$m measurement is the de-boosted flux from Perera et al. (2008; AzGN36).

[b] The 100 $\mu$m, 250 $\mu$m, 350 $\mu$m, and 500 $\mu$m fluxes were measured by us using the publicly available *Herschel* data. The 860 $\mu$m flux is from this paper. The 1100 $\mu$m measurement is the de-boosted flux from Perera et al. (2008; AzGN03).

[c] The 24 $\mu$m flux is from Magnelli et al. (2011). The separation between the 24 $\mu$m source position and the SMA position is $0.91''$. The 160 $\mu$m, 250 $\mu$m, 350 $\mu$m, and 500 $\mu$m fluxes were measured by us using the publicly available *Herschel* data. The 860 $\mu$m flux is from this paper. The 1100 $\mu$m measurement is the de-boosted flux from Perera et al. (2008; AzGN05).

[d] The 24 $\mu$m flux is from Magnelli et al. (2011). The separation between the 24 $\mu$m source position and the SMA position is $0.22''$. The 160 $\mu$m, 250 $\mu$m, and 350 $\mu$m fluxes are from Magnelli et al. (2012). The 860 $\mu$m flux is from this paper. The 1100 $\mu$m measurement is the de-boosted flux from Perera et al. (2008; AzGN16).

[e] The 24 $\mu$m flux is from Magnelli et al. (2011). The separation between the 24 $\mu$m source position and the SMA position is $0.31''$. Note that the 24 $\mu$m flux listed in Magnelli et al. (2012) is that of a more distant source (separation $2.96''$), since they did not have the accurate SMA position. The 160 $\mu$m, 250 $\mu$m, 350 $\mu$m, and 500 $\mu$m fluxes are from Magnelli et al. (2012). The 860 $\mu$m flux is from this paper.

et al. (1997) modified blackbody fit to Arp 220 with $\beta = 1$ and a dust temperature of $T_d = 47$ K to represent their 850 $\mu$m-selected SCUBA sources. Even for our clean SMA sample sources, which have considerably better wavelength coverage than the Barger et al. sources had, this fit provides a very good representation of the data (black curve in Figure 8). Of course, since galaxies do not have single temperatures, such a fit can, at best, only represent an emission-weighted global average. In Figure 8(a), we normalized the modified blackbody fit to GOODS 850-6, the one source with only a millimetric redshift, which is why the radio point for this source lies directly on the synchrotron relation. In Figure 8(b), we normalized the SMGs to Arp 220 at rest-frame 100 $\mu$m, the peak of the distribution where the SEDs are relatively flat. It is clear from both plots how similar the distant SEDs are to Arp 220.

As noted above, $\beta$ is determined empirically. Dunne & Eales (2001) found a constant value of $\beta \sim 2$ for a sample of local galaxies selected from the *IRAS* Bright Galaxy Sample that they observed with SCUBA, while Casey et al. (2011) found values ranging from $\beta \sim 1 - 2.5$ for a sample of 250 $\mu$m-selected luminous galaxies at $z > 1$ found with the Balloon-borne Large-Aperture Submillimeter Telescope (BLAST; Pascale et al. 2008).

Assuming $\beta$ to be universal, Magnelli et al. (2012) performed a global fit using their sample of 61 SMGs by gridding the $\beta$ parameter space of $0.1 - 3.0$ in steps of 0.05. They then did a $\chi^2$ minimization at each $\beta$ by varying $T_d$ and the blackbody normalization. They defined the $\chi^2$ value at a given $\beta$ to be the sum of the individual $\chi^2_{\rm gal}$ values. They applied their global fit to three wavelength ranges. They found $\beta$ values of $0.6 \pm 0.2$, $1.2 \pm 0.2$, and $1.7 \pm 0.3$ for, respectively, 70 $\mu$m to the submillimeter, the same, except excluding the *Herschel*-PACS 70 $\mu$m and 100 $\mu$m data, and the same, except excluding the *Herschel*-PACS 70 $\mu$m, 100 $\mu$m, and 160 $\mu$m data. This observed increase in $\beta$ when excluding shorter wavelength data led them to conclude that constraints on $\beta$ are very sensitive to the wavelength coverage used in the fits, as well as to the noise properties of the observations.

Casey (2012) argued that she could constrain $\beta$ with $> 3$ independent photometric points at rest-frame $\lambda \geq 200$ $\mu$m when she used her simultaneous fit to a graybody and an MIR power law. When such data are not available, however, she recommended adopting a fixed value of $\beta = 1.5$, which is a common approach at high redshifts (e.g., Chapman et al. 2005; Kovács et al. 2006; Pope et al. 2006; Hwang et al. 2010).

Here we perform fits to the long-wavelength SEDs of our clean SMA sample using a modified blackbody and allowing the values of $\beta$ and $T_d$ to vary. In Figure 9, we show the resulting fits for the sources. We find a mean value of $\beta = 1.29$ and a mean value of $T_d = 42.9$ K for the sample. If we instead fix $\beta = 1.5$, then we find $T_d = 36.2$, 46.1, 39.1, 43.1, 37.0 K for GOODS 850-3 (GN05), GOODS 850 5 (GN10), GOODS 850-6, GOODS 850-7 (GN04), and GOODS 850-9 (GN19), respectively. For $\beta = 1.0$, we find $T_d = 42.6$, 54.7, 45.4, 50.7, and 41.9 K, with an average value of 47.1 K. This is nearly identical to the Arp 220 value of 47 K when it is fitted in the same way.

### 5.2. *The High-Redshift FIR-Radio Correlation*

The FIR-radio correlation is usually parameterized by the quantity $q$ (e.g., Helou et al. 1985, 1988; Condon et al. 1991), which is defined as

$$q = \log\left(\frac{L_{\rm FIR}}{3.75 \times 10^{12}\ {\rm erg\ s^{-1}}}\right) - \log\left(\frac{P_{1.4\ {\rm GHz}}}{{\rm erg\ s^{-1}\ Hz^{-1}}}\right), \quad (1)$$

where $L_{\rm FIR}$ is the FIR luminosity, and $P_{1.4\ {\rm GHz}}$ is the rest-frame 1.4 GHz power. Here we compute the FIR luminosities over the rest-frame wavelength range $42.5 - 122.5$ $\mu$m, which is fully covered by the data (i.e., we did the computations using the blue regions of the fits in Figure 9, though we obtained identical luminosities when we interpolated the data instead), rather than the infrared luminosities over the rest-frame wavelength range $8 - 1000$ $\mu$m (e.g., Kennicutt 1998; Bell 2003; Ivison et al.

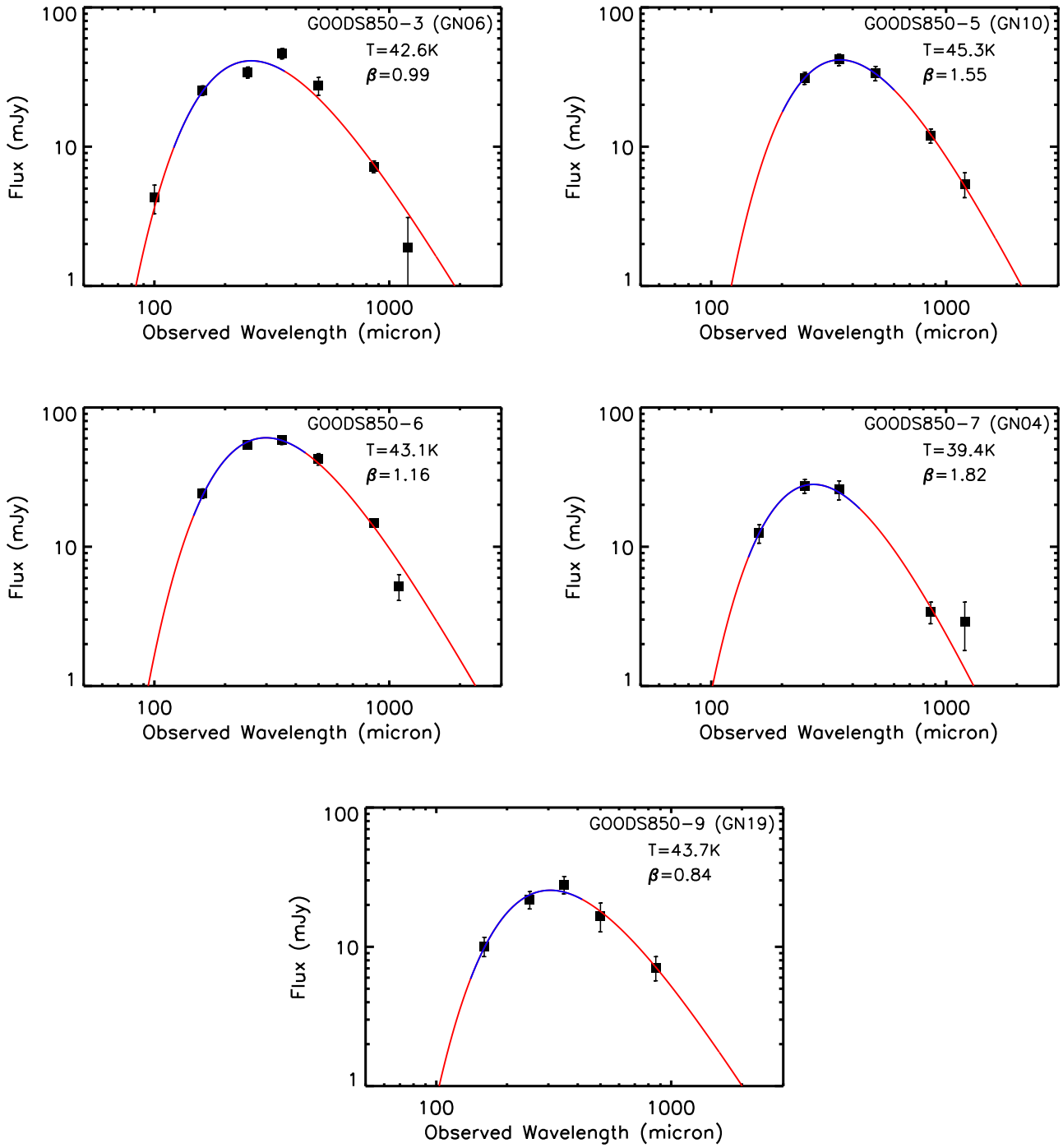



FIG. 9.— Modified blackbody fits (red curves) to the SEDs of the 5 SMGs (black squares) in our clean SMA sample, allowing $\beta$ and $T_d$ to vary. The regions corresponding to rest-frame 42.5 − 122.5 $\mu$m are shown in blue in each of the panels, since that is the wavelength range of the fits used to measure FIR luminosities in Section 5.2. The data are taken fom Table 6, and the error bars are $\pm 1\sigma$. The best-fit values of $\beta$ and $T_d$ are shown in the upper right corner of each panel.

2010a, b), which would require uncertain extrapolations. This also allows us to compare directly with many of the lower redshift analyses that also use $42.5-122.5$ $\mu$m (e.g., Yun et al. 2001). We compute the rest-frame radio power assuming $S_\nu \propto \nu^\alpha$ and a radio spectral index of $\alpha = -0.8$ (Condon 1992; Ibar et al. 2010); that is,

$$P_{1.4\ \mathrm{GHz}} = 4\pi {d_L}^2 S_{1.4\ \mathrm{GHz}} 10^{-29} (1+z)^{\alpha-1}\ \mathrm{ergs\ s^{-1}\ Hz^{-1}}. \quad (2)$$

Here $d_L$ is the luminosity distance (cm) and $S_{1.4\ \mathrm{GHz}}$ is the 1.4 GHz flux density ($\mu$Jy). The choice of $\alpha$ may not be appropriate for AGN and also may be problematic for high-redshift sources. However, we note that, because we calibrate the relation between the FIR luminosity and the radio power using this assumption, the final star formation rate calibrations do not depend on this choice, though the $q$ values, which represent the intermediate step in the process, do.

At very high redshifts, this relation must begin to break down, because the Compton cooling of the relativistic electrons on the CMB, which increases rapidly with increasing redshift, will begin to dominate over synchrotron losses (e.g., Condon 1992). This will decrease the radio power and increase the value of $q$. The crossover point occurs when the energy density in the CMB becomes comparable to the magnetic field energy density in the galaxy. For the ULIRGs of the present sample, where the magnetic field and relativistic energy density are expected to be extremely high, this may not occur over the observed redshift range.

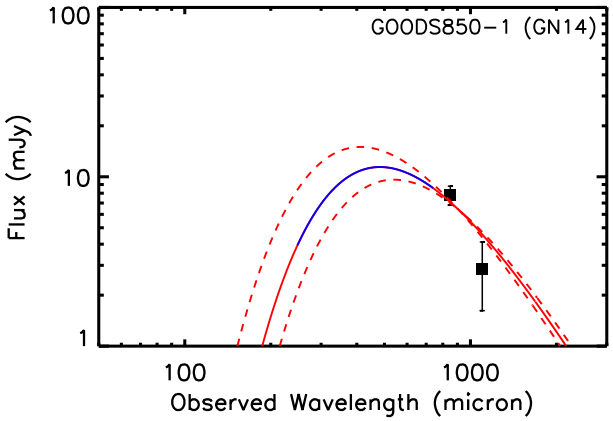



FIG. 10.— Modified blackbody fit to the 860 $\mu$m and 1100 $\mu$m data of GOODS 850-1 (GN14/HDF850.1). The normalization was obtained by assuming $\beta = 1$ and a temperature of 47 K (red solid curve). We also show the fits when the temperature is varied from 42 K to 55 K while keeping $\beta = 1$ (red dashed curves). The region corresponding to rest-frame $42.5-122.5$ $\mu$m is shown in blue, since that is the wavelength range of the fit used to measure the FIR luminosity.

We did not include GOODS 850-1 (GN14/HDF850.1) in our clean SMA sample, because the *Herschel* fluxes are too low to be confidently measured (see Figure A1). However, at the known $z = 5.183$ redshift of the source (Walter et al. 2012), the observed-frame 860 $\mu$m lies close to the rest-frame $42.5-122.5$ $\mu$m band, which means we can strongly constrain the $q$ value even without the *Herschel* data. In Figure 10, we show fits to our 860 $\mu$m SMA data and the 1100 $\mu$m data ($2.87 \pm 1.25$) from Chapin et al. (2009; their Table A3) assuming $\beta = 1$ and $T = 47$ K (red solid curve) or $\beta = 1$ and the range $T = 42$ to 55 K (red dashed curves). The corresponding value of q is 2.34 with a range from 2.22 to 2.50. The calculated q values are not sensitive to the choice of $\beta$ and the range is primarily determined by our assumption that the dust temperature is similar to those at the lower redshifts of our clean SMA sample. Using $\beta = 1.5$ would change the q range by approximately 0.01.

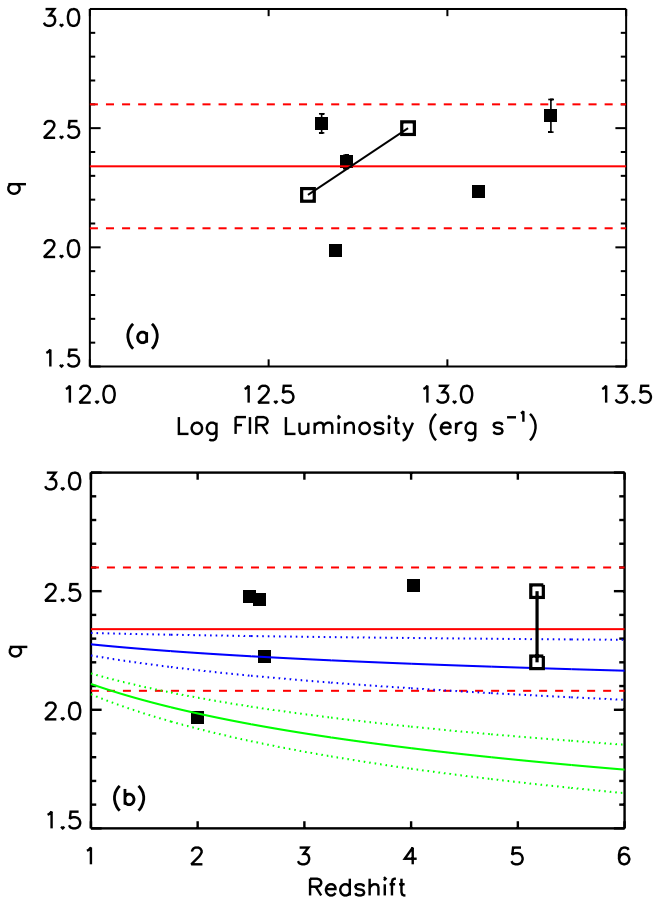



FIG. 11.— (a) $q$ values and $\pm 1\sigma$ error bars for the 5 SMGs in our clean SMA sample (black squares) vs. their (a) FIR luminosities and (b) redshifts. The $q$ values correspond to the FIR luminosities computed over the rest-frame wavelength range $42.5-122.5$ $\mu$m, which is fully covered by the data. The open squares show the range of $q$ values and FIR luminosities obtained for GOODS 850-1 (GN14/HDF850.1), assuming $\beta = 1$ and a range of temperatures from $T = 42-55$ K. In each panel, the red solid line shows the local $\langle q \rangle$ value from Yun et al. (2001), and the red dashed lines indicate the scatter that Yun et al. observed in their FIR-radio correlation. In panel (b), the green solid curve with dotted $\pm 1\sigma$ uncertainties shows the redshift evolution of $\langle q \rangle \propto (1+z)^{-0.15\pm0.03}$ obtained by Ivison et al. (2010a) from a stacking analysis using *Spitzer* and *BLAST* data in the ECDFS, and the blue solid curve with dotted $\pm 1\sigma$ uncertainties shows the redshift evolution of $\langle q \rangle \propto (1+z)^{-0.04\pm0.03}$ obtained by Ivison et al. (2010b) from a stacking analysis using *Spitzer* and *Herschel* data in the GOODS-N.

In Figure 11, we plot the $q$ values that we calculated for the 5 SMGs in our clean SMA sample versus (a) the logarithm of their FIR luminosities and (b) their redshifts. From an *IRAS* Redshift Survey sample identified in the NRAO VLA Sky Survey catalog, Yun et al. (2001) found a local value of $\langle q \rangle = 2.34 \pm 0.01$ (red solid line) and

a scatter in the linear FIR-radio correlation of 0.26 dex (red dashed lines). Our SMGs have $q$ values consistent with this local range, with an average value of $\langle q \rangle = 2.36$ over the redshift range from $z = 2-4.2$. For an Arp 220 SED, the value of the FIR luminosity calculated over $8-1000$ $\mu$m is 1.42 times the $42.5-122.5$ $\mu$m value, giving $\langle q(8-1000) \rangle = 2.51 \pm 0.01$, which may be compared with the local value of $\langle q \rangle = 2.52$ found by Bell (2003).

In Figure 11(a) and (b), we also show the range in $q$ values and FIR luminosities (connected open squares) for GOODS 850-1 (GN14/HDF850.1) that we calculated above assuming $\beta = 1$. We do not use these in our subsequent analysis, but they suggest that the invariance in $q$ seen for these high-luminosity galaxies extends to beyond $z = 5$.

Although many authors have tried to investigate whether the FIR-radio correlation continues to hold to high redshifts using infrared data from *ISO* to *SHARC-2* to *Spitzer* to *BLAST* to *Herschel* (e.g., Garrett 2002; Appleton et al. 2004; Kovács et al. 2006; Ibar et al. 2008; Garn et al. 2009; Sargent et al. 2010a, 2010b; Seymour et al. 2009; Ivison et al. 2010a, b; Magnelli et al. 2012), their conclusions have varied. A major concern for many of these studies is whether radio pre-selection may be biasing their results.

Our data extend to higher redshifts than most of these studies and are not subject to a radio bias, since all of our sources are detected in the radio image. Parameterizing the $q$ values for the 5 SMGs in our clean SMA sample as evolving as $(1+z)^{\gamma}$ (we normalized to the Yun et al. 2001 value locally), we find $\gamma = 0.01 \pm 0.03$, which is consistent with no evolution. For comparison, Ivison et al. (2010a) performed a stacking analysis using *BLAST* data on the Extended *Chandra* Deep Field South (ECDFS) at the positions of MIR-selected galaxies from *Spitzer* with photometric redshifts and found $\gamma = -0.15 \pm 0.03$ (green solid curve with dotted $\pm 1\sigma$ uncertainties) in Figure 11(b)). Likewise, Ivison et al. (2010b) performed a stacking analysis using *Herschel* data on the GOODS-N at the positions of MIR-selected galaxies from *Spitzer* spanning $z = 0-2$ and matched in infrared luminosity ($10^{11}-10^{12}$ $L_{\odot}$) and found $\gamma = -0.04 \pm 0.03$ (blue solid curve with dotted $\pm 1\sigma$ uncertainties).

## 6. THE FORMATION HISTORY OF EXTREME STAR-FORMING GALAXIES

The detection in the radio of every source in our SMA sample, together with a high fraction of spectroscopically identified sources stretching out to $z = 5.18$, as well as millimetric redshifts for all of the remaining sources, provide us with a sample where we can measure the star formation rates (SFRs) per comoving volume to high redshifts and compare them with those determined from extinction-corrected ultraviolet-selected populations.

If we assume that the FIR-radio correlation is roughly invariant for the SMGs with redshifts from $z \approx 0-5$, then we can compute the SFRs for the individual sources from the 1.4 GHz power. We caution, however, that we only showed in Section 5.2 that this invariance holds at $z = 2-4.2$ for the more luminous SMGs where we are able to measure the *Herschel* fluxes. Thus, here we have to assume that our results extend down to our 860 $\mu$m flux threshold of 3 mJy, which is about a factor of 2 lower than the fluxes of the sources with measured FIR luminosities from the *Herschel* data, and that our results apply out to $z = 5.18$, where we have less information.

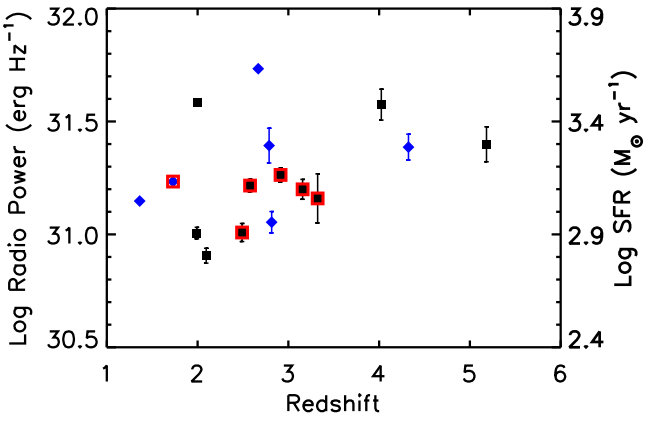



FIG. 12.— Radio power vs. redshift. Sources with spectroscopic redshifts are shown with black squares. Other sources are shown with blue diamonds at the millimetric redshift. The right-hand axis shows the corresponding SFR computed from Equation 3 with A= −28.1. SMGs with X-ray detections are marked with red boxes.

In Figure 12, we show the radio power of the SMGs in our SMA sample versus redshift. We denote sources with spectroscopic redshifts with black squares and sources with only millimetric redshifts as blue diamonds. We convert the radio power to a SFR using the equation,

$$\log \mathrm{SFR}(\mathrm{M}_{\odot}\ \mathrm{yr}^{-1}) = \log P_{1.4\ \mathrm{GHz}}\ (\mathrm{ergs\ Hz}^{-1}) - A\,. \quad (3)$$

The SFR is for a Salpeter (1955) initial mass function (IMF) from $0.1-100$ $\mathrm{M}_{\odot}$.

The normalizing constant $A$ can be calculated from the $q$ value if we have a relation between the FIR luminosity and the SFR. Bell (2003) used the Kennicutt (1998) relation between the FIR ($8-1000$ $\mu$m) and the SFR. Applying a small correction for the contribution of old stars to the FIR, they found $A = 28.26$. Our results show that this can be applied to high redshifts. However, this normalization is about a factor of two lower than Condon (1992) computed based on the Milky Way. The factor of two range is probably a reasonable measure of the systematic uncertainty in the SFR versus FIR luminosity relation. Following Cowie et al. (2012), we adopt an intermediate normalization of $A = 28.1$.

We show the SFRs on the right-hand axis in Figure 12. The values range from $700-5000$ $\mathrm{M}_{\odot}$ yr$^{-1}$. Since the galaxies were selected in the submillimeter, and all are detected in the radio, the use of the radio power to compute the SFRs should not introduce any selection biases. Indeed, there are no signs of any strong dependences of the SFRs on redshift in Figure 12.

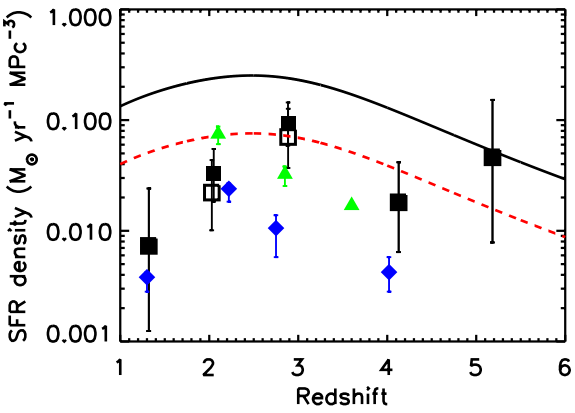



FIG. 13.— SFR per unit comoving volume vs. redshift for our SMA sample (black filled squares). The data points are shown at the mean redshift of the SMGs in each redshift bin. The error bars are $\pm1\sigma$ based on the Poissonian distribution corresponding to the number of sources in each bin. These points are not corrected for completeness and only represent SMGs with 860 $\mu$m fluxes above 3 mJy. Thus, they should be considered as lower limits. The black open squares show our results after removing five sources with X-ray detections that could be dominated by AGNs (see text for details). The black curve shows the SFR density history from Hopkins & Beacom (2006). We scaled their modified Salpeter IMF to our Salpeter IMF. The red dashed curve shows the Hopkins & Beacom curve renormalized by a factor of 0.3 to match our SMG-inferred value in the $z = 2 - 3$ bin. The green triangles show the results of Chapman et al. (2005), and the blue diamonds show the results of Wardlow et al. (2011), with $1\sigma$ uncertainties. In both cases, we increased the normalization of their points by a factor of 1.4 to match our assumed SFR conversion.

Now we can determine the contributions of the SMGs to the SFR per unit comoving volume (hereafter, SFR density) as a function of cosmic time. The area over which each of the SMGs is detected is the area over which a SCUBA source of that 850 $\mu$m flux could have been detected at the $4\sigma$ level in the original survey of W04. For the SCUBA sources that turned out to be multiple SMA sources, the appropriate area for each of the individual SMA sources is the area corresponding to the total SCUBA flux for the composite source.

We next determined the SFR density in five redshift bins of size unity over the redshift range $z = 0.5$ to 5.5. To do this, we took the individual SFRs in a particular redshift bin, divided each by the comoving volume in that redshift bin calculated using the surveyed area for that particular object, and summed them. (Note that the SMG flux relative to the FIR luminosity is insensitive to redshift.) We show our results in Figure 13 as black filled squares with error bars that are determined from the number of sources in each bin. We note that while the SFRs of individual sources (see Figure 12) could be affected by gravitational lensing, the SFR density would not change, because lensing is surface brightness conserving, and the surveyed area scales with the change in the SFR of the galaxy. However, if lensing were significant, then the measured SFR density could include the contributions from more numerous fainter galaxies that lie below the survey limits.

We compare our results with previous work based on SMG samples by Chapman et al. (2005, green triangles) and Wardlow et al. (2011, blue diamonds). These authors used the same cosmology and Salpeter IMF that we used. We increased the normalization of their points by a factor of 1.4 to match our assumed SFR conversion. The Chapman et al. SMGs with radio counterparts have spectroscopic redshifts for the most part. They put their SMGs without radio counterparts into the $z = 3 - 4$ bin. The counterparts to the Wardlow et al. SMGs come from radio, *Spitzer* 24 $\mu$m, and *Spitzer* IRAC data and have mostly photometric redshifts. In the $z = 2 - 3$ bin, our results agree well with those of Chapman et al. The results of Wardlow et al. in this redshift bin are slightly low, but this can be partly understood as a consequence of the slightly higher flux threshold used by Wardlow et al. (an 870 $\mu$m flux of 4 mJy). Wardlow et al. also suggest that their results may be low due to the ECDFS area being underdense (Weiß et al. 2009). In both cases, the Chapman et al. and the Wardlow et al. results fall below our results at higher redshifts. This is easily understood as a consequence of the selection bias introduced in their measurements by the radio flux limits of their data, which result in the high-redshift sources being omitted.

One of the most difficult issues in deriving the star formation history is determining the contribution of AGNs to the FIR luminosity. In computing the points in Figure 13, we have assumed that, even when AGN activity is present, it is not the dominant contributor to the FIR luminosity. This is similar to the assumption made by Wardlow et al. (2011). In contrast, Chapman et al. (2005) reduced their results by 30% to allow for possible AGN contributions. Six of our SMA sources contain AGNs based on their X-ray luminosities, but in the case of GOODS 850-12 (GN15/HDF850.2), the radio emission is extended, suggesting the primary power source may be star formation (see Table 5). If we assume the FIR luminosities of the remaining five sources with X-ray detections are dominated by the AGN, then that would reduce the SFR per unit comoving volume in the $z = 1-4$ range by a factor of 1.3 (black open squares). This would also slightly flatten the star formation history, since it is primarily the intermediate redshift bins that are affected. There may be some extremely Compton-thick AGNs that are not picked up by the X-ray selection. However, of the 10 sources that are not X-ray AGNs in the SMA sample, 3 are extended radio sources (Table 5 lists 3; Momjian et al. 2010 has GOODS 850-3 in common with Table 5), suggesting that at least in these cases the FIR luminosities are primarily powered by star formation.

We can now compare our SFR density history with that of Hopkins & Beacom (2006; we scaled their modified Salpeter IMF to our Salpeter IMF), a compilation that is often used as a reference (black curve). At the redshifts of interest ($z > 2$), the Hopkins & Beacom results are based on extinction corrected ultraviolet samples using a common extinction correction. We find that the contribution of our SMG sample is about 30% (red dashed curve) of the Hopkins & Beacom SFR density. Our SFR density is strictly a lower limit to the contribution from the overall SMG population, since we have not corrected for incompleteness in the original sample (both missing sources in the observed flux range and sources that lie below the 3 mJy flux limit). However, even the present results show that over the redshift range $z = 1 - 6$, a large and relatively invariant fraction of the overall SFR density is contained in these massively star-forming galaxies. It should be em-

phasized that the present star-forming galaxies will only be partly included in an extinction-corrected ultraviolet selected sample, such as that of Hopkins & Beacom. Excluding GOODS 850-17, where the neighboring bright galaxy contaminates the photometry, 7 of the 15 sources have F850LP magnitudes fainter than 26, 4 of which are not detected at all in the GOODS ACS data. Thus, roughly half of the star formation seen in this SMA sample would not have been included in an ultraviolet star formation estimate. Thus, determinations of the star formation history from extinction-corrected ultraviolet selected populations and from SMG-selected populations are only partially overlapping and need to be combined, allowing for the overlap.

## 7. SUMMARY

In this paper, we presented our extremely sensitive (sub-mJy rms) SMA 860 $\mu$m continuum imaging survey of a complete sample of highly significant ($> 4\sigma$) SCUBA 850 $\mu$m sources with fluxes above 3 mJy that were detected in the W04 survey of the GOODS-N. Using our SMA observations, as well as SCUBA-2 observations of the field obtained by C13, we did not detect 4 of the sources in the sample, and we ruled out the original SCUBA fluxes for those sources at the $4\sigma$ level. Using the SCUBA-2 data, we also did not detect a similar number of highly significant sources in the P05 SCUBA sample. It is quite common in the literature to see studies that include SMGs detected at significances lower than $4\sigma$; however, our study illustrates the dangers of including such sources and emphasizes the need for caution even when analyzing highly significant SCUBA samples, if there are are no confirming submillimeter data available.

More intriguingly, we found that 3 of the SCUBA sources in the sample resolved into multiple, fainter SMGs. We concluded that the positional accuracy that one obtains from interferometric submillimeter or millimeter observations is absolutely critical for making correct counterpart identifications and that those identifications made at wavebands far from the detection waveband or using low spatial resolution data may be highly misleading.

We used new ultradeep 20 cm data of the field obtained by Owen13 with the upgraded VLA to find $> 5\sigma$ radio counterparts to all of the sources in our SMA sample. We used these data to estimate millimetric redshifts, though we found that the bulk of the sources in our sample (10/16) already had spectroscopic redshifts in the literature.

We constructed SEDs for a clean sample of 5 SMGs that were isolated (so accurate flux measurements could be made) and had *Herschel* data, which provided the critical measurements at the peak of the thermal dust spectrum. We found these SEDs to be very similar to that of the local ULIRG Arp 220.

Using the SEDs, we measured FIR luminosities for the 5 SMGs over the wavelength range 42.5-122.5 $\mu$m covered by the data. We used these FIR luminosities together with the radio power of the sources to determine $q$, the usual parameterization of the FIR-radio correlation, for each source. We included one additional source at $z = 5.183$, whose 860 $\mu$m flux is close enough to the peak of the thermal dust spectrum to be strongly constraining of $q$, even without *Herschel* data, and saw it was also consistent with no evolution in the FIR-radio correlation with redshift. Our sample is not subject to the radio bias that has plagued many earlier studies on this topic. We found that our sources had $q$ values consistent with the local range out to redshifts beyond 5.

With the detection of our entire SMA sample in the radio and the advantage of having a high fraction of spectroscopic redshifts, we were able to measure the evolution of the SFR density with redshift for our sample and compare it with that determined from ultraviolet-selected populations. These are the first reliable measurements at high redshifts, since previous results have been highly biased against such objects due to the radio selection needed to localize the sources. We found that the contribution from our sample to the overall SFR density is a substantial and fairly invariant fraction of about 30% of the Hopkins & Beacom (2006) extinction-corrected ultraviolet selected compilation over the redshift range $z = 1 - 6$. We emphasize that determinations of the star formation history from extinction-corrected ultraviolet selected populations and from SMG-selected populations are only partially overlapping, due to the extreme ultraviolet faintness of some of the SMGs.

We thank Steve Serjeant for a thoughtful review of the paper. We thank Y.-W. Tang and the SMA staff for help in acquiring the data and M. A. Gurwell for help with the data reduction. We gratefully acknowledge support from the University of Wisconsin Research Committee with funds granted by the Wisconsin Alumni Research Foundation and the David and Lucile Packard Foundation (A. J. B.), NSF grant AST-0709356 (L. L. C.), and National Science Council of Taiwan grant 99-2112-M-001-012-MY3 (W.-H. W.). This research has made use of data from the HerMES project (http://hermes.sussex.ac.uk/). HerMES is a Herschel Key Programme utilising Guaranteed Time from the SPIRE instrument team, ESAC scientists, and a mission scientist. HerMES are described in Oliver et al. (2012). The HerMES data were accessed through the HeDaM database (http://hedam.oamp.fr) operated by CeSAM and hosted by the Laboratoire d'Astrophysique de Marseille.

## REFERENCES

Alexander, D. M., et al. 2003a, AJ, 125, 383
Alexander, D. M., et al. 2003b, AJ, 126, 539
Appleton, P. N., et al. 2004, ApJ, 154, 147
Aretxaga, I., et al. 2011, MNRAS, 415, 3831
Austermann, J. E., et al. 2010, MNRAS, 401, 160
Barger, A. J., Cowie, L. L., Mushotzky, R. F., & Richards E. A. 2001a, ApJ, 121, 662
Barger, A. J., Cowie, L. L., & Richards, E. A. 2000, AJ, 119, 2092
Barger, A. J., Cowie, L. L., & Sanders, D. B. 1999, ApJ, 518, L5
Barger, A. J., Cowie, L. L., Sanders, D. B., Fulton, E., Taniguchi, Y., Sato, Y., Kawara, K., & Okuda, H. 1998, Nature, 394, 248
Barger, A. J., Cowie, L. L., Steffen, A. T., Hornschemeier, A. E., Brandt, W. N., & Garmire, G. P. 2001b, ApJ, 560, L23
Barger, A. J., Cowie, L. L., & Wang, W.-H. 2008, ApJ, 689, 687
Bautz, M. W., Malm, M. R., Baganoff, F. K., Ricker, G. R., Canizares, C. R., Brandt, W. N., Hornschemeier, A. E., & Garmire, G. P. 2000, ApJ, 543, L119
Bell, E. F. 2003, ApJ, 586, 794
Bertoldi, F., et al. 2007, ApJS, 172, 132

Blain, A. W., Kneib, J.-P., Ivison, R. J., & Smail, I. 1999, ApJ, 512, L87
Blain, A. W., & Longair, M. 1993, MNRAS, 265, L21
referenceborys03 Borys, C., Chapman, S., Halpern, M., & Scott, D. 2003, MNRAS, 344, 385
Bothwell, M. S., et al. 2010, MNRAS, 405, 219
Bothwell, M. S., et al. 2012, MNRAS, submitted (arXiv:1205.1511)
Briggs, D. S. 1995, BAAS, 27, 1444
Capak, P. L., et al. 2008, ApJ, 681, L53
Capak, P. L., et al. 2011, Nature, 470, 233
Carilli, C. L., & Yun, M. S. 1999, ApJ, 513, L13
Casey, C. M. 2012, MNRAS, 425, 3094
Casey, C. M., Chapman, S. C., Smail, I., Alaghband-Zadeh, S., Bothwell, M. S., & Swinbank, A. M. 2011, MNRAS, 411, 2739
Chapin, E. L., et al. 2009, MNRAS, 398, 1793
Chapman, S. C., et al. 2003a, Nature, 422, 695
Chapman, S. C., et al. 2003b, ApJ, 585, 57
Chapman, S. C., Smail, I., Windhorst, R., Muxlow, T., & Ivison, R. J. 2004, ApJ, 611, 732
Chapman, S. C., et al. 2005, ApJ, 622, 772
Chen, C.-C., Cowie, L. L., Wang, W.-H., Barger, A. J., & Williams, J. P. 2011, ApJ, 733, 64
Clements, D. L., et al. 2008, MNRAS, 387, 247
Condon, J. J., Anderson, M. L., & Helou, G. 1991, ApJ, 376, 95
Condon, J. J. 1992, ARA&A, 30, 575
Coppin, K., et al. 2006, MNRAS, 372, 1621
Coppin, K. E. K., et al. 2009, MNRAS, 395, 1905
Coppin, K. E. K., et al. 2010, MNRAS, 407, L103
Cowie, L. L., Barger, A. J., & Hu, E. M. 2011, ApJ, 738, 136
Cowie, L. L., Barger, A. J., & Kneib, J.-P. 2002, AJ, 123, 2197
Cowie, L. L., Barger, A. J., Wang, W.-H., & Williams, J. P. 2009, ApJ, 697, L122
Cowie, L. L., Hu, E. M., & Songaila, A. 1995, AJ, 110, 1576
Daddi, E., Dannerbauer, H., Krips, M., Walter, F., Dickinson, M., Elbaz, D., & Morrison, G. E. 2009a, ApJ, 695, L176
Daddi, E., et al. 2009b, ApJ, 694, 1517
Dannerbauer, H., Lehnert, M. D., Lutz, D., Tacconi, L., Bertoldi, F., Carilli, C., Genzel, R., & Menten, K. M. 2004, ApJ, 606, 664
Dannerbauer, H., et al. 2010, ApJ, 720, L144
Dannerbauer, H., Walter, F., & Morrison, G. 2008, ApJ, 673, L127
Downes, D., et al. 1999, A&A, 347, 809
Dunne, L., & Eales, S. A. 2001, MNRAS, 327, 697
Eales, S., Lilly, S., Gear, W., Dunne, L., Bond, J. R., Hammer, F., Le Fèvre, O., & Crampton, D. 1999, ApJ, 515, 518
Eales, S., Lilly, S., Webb, T., Dunne, L., Gear, W., Clements, D., & Yun, M. 2000, AJ, 120, 2244
Eddington, A. S. 1913, MNRAS, 73, 359
Ezawa, H., Kawabe, R., Kohno, K., & Yamamoto, S. 2004, SPIE, 5489, 763
Fixsen, D. J., Dwek, D., Mather, J. C., Bennett, C. L., & Shafer, R. A. 1998, ApJ, 508, 123
Fomalont, E. B., Kellermann, K. I., Cowie, L. L., Capak, P., Barger, A. J., Partridge, R. B., Windhorst, R. A., & Richards, E. A. 2006, ApJS, 167, 103
Garn, T., Green, D. A., Riley, J. M., & Alexander, P. 2009, MNRAS, 397, 1101
Garrett, M. A. 2002, A&A, 384, L19
Giavalisco, M., et al. 2004, ApJ, 600, L93
Grève, T. R., Ivison, R. J., Bertoldi, F., Stevens, J. A., Dunlop, J. S., Lutz, D., & Carilli, C. L. 2004, MNRAS, 354, 779
Grève, T. R., Pope, A., Scott, D., Ivison, R. J., Borys, C., Conselice, C. J., & Bertoldi, F. 2008, MNRAS, 389, 1489
Güsten, R., et al. 2006, SPIE, 6267, 626714
Hatsukade, B., et al. 2010, ApJ, 711, 974
Hauser, M. G., et al. 1998, ApJ, 508, 25
Helou, G., Khan, I. R., Malek, L, & Boehmer, L. 1988, ApJS, 68, 151
Helou, G., Soifer, B. T., & Rowan-Robinson, M. 1985, ApJ, 298, L7
Ho, P. T. P., Moran, J. M., & Lo, K. Y. 2004, ApJ, 616, L1
Holland, W. S., et al. 1999, MNRAS, 303, 659
Hopkins, A. M., & Beacom, J. F. 2006, ApJ, 651, 142
Hughes, D. H., et al. 1998, Nature, 394, 241
Hwang, H. S., et al. 2010, MNRAS, 409, 75
Ibar, E., et al. 2008, MNRAS, 386, 953
Ibar, E., Ivison, R. J., Best, P. N., Coppin, K., Pope, A., Smail, I., & Dunlop, J. S. 2010, MNRAS, 401, L53
Iono, D., et al. 2006, ApJ, 640, L1
Ivison, R. J., et al. 2002, MNRAS, 337, 1
Ivison, R. J., et al. 2007, MNRAS, 380, 199
Ivison, R. J., et al. 2010a, MNRAS, 402, 245
Ivison, R. J., et al. 2010b, A&A, 518, L31
Johansson, D., Sigurdarson, H., & Horellou, C. 2011, A&A, 527, 117
Karim, A., et al. 2012, MNRAS, submitted (arXiv:1210.0249)
Kennicutt, R. C. 1998, ApJ, 498, 541
Klaas, U., Haas, M., Heinrichsen, I., & Schulz, B. 1997, A&A, 325, L21 (1997)
Knudsen, K. K., Kneib, J.-P., Richard, J., Petitpas, G., & Egami, E. 2010, ApJ, 709, 210
Knudsen, K. K., van der Werf, P. P., & Kneib, J.-P. 2008, MNRAS, 384, 1611
Kovács, A., Chapman, S. C., Dowell, C. D., Blain, A. W., Ivison, R. J., Smail, I., & Phillips, T. G. 2006, ApJ, 650, 592
Kreysa, E., et al. 1998, Proc. SPIE, 3357, 319
Lagache, G., Puget, J.-L., & Dole, H. 2005, ARA&A, 43, 727
Larson, D., et al. 2011, ApJS, 192, 16
Lindner, R. R., et al. 2011, ApJ, 737, 83
Magnelli, B., Elbaz, D., Chary, R. R., Dickinson, M., Le Borgne, D., Frayer, D. T., & Willmer, C. N. A. 2011, A&A, 528, A35
Magnelli, B., et al. 2012, A&A, 539, id.A155
Michałowski, M. J., et al. 2012, MNRAS, 426, 1845
Momjian, E., Wang, W.-H., Knudsen, K. K., Carilli, C. L., Cowie, L. L., & Barger, A. J. 2010, AJ, 139, 1622
Morrison, G. E., Owen, F. N., Dickinson, M., Ivison, R. J., & Ibar, E. 2010, ApJS, 188, 178
Oliver, S., et al. 2012, MNRAS, 424, 1614
Owen, F. N., & Morrison, G. E. 2008, AJ, 136, 1889
Pascale, E., et al. 2008, ApJ, 681, 400
Perera, T. A., et al. 2008, MNRAS, 391, 1227
Pope, A., Borys, C., Scott, D., Conselice, C., Dickinson, M., & Mobasher, B. 2005, MNRAS, 358, 149 (P05)
Pope, A., et al. 2006, MNRAS, 370, 1185
Pope, A., et al. 2008, ApJ, 675, 1171
Puget, J.-L., Abergel, A., Bernard, J.-P., Boulanger, F., Burton, W. B., Désert, F.-X., & Hartmann, D. 1996, A&A, 308, L5
Riechers, D. A., et al. 2010, ApJ, 720, L131
Reddy, N. A., Steidel, C. C., Erb, D. K., Shapley, A. E., & Pettini, M. 2006, ApJ, 653, 1004
Salpeter, E. E. 1955, ApJ, 121, 161
Sargent, M. T., et al. 2010a, ApJS, 186, 341
Sargent, M. T., et al. 2010b, ApJ, 714, L190
Schinnerer, E., et al. 2008, ApJ, 689, L5
Scott, K. S., et al. 2008, MNRAS, 385, 2225
Scott, K. S., et al. 2010, MNRAS, 405, 2260
Scott, K. S., et al. 2012, MNRAS, 423, 575
Scott, S. E., et al. 2002, MNRAS, 331, 817
Serjeant, S., et al. 2003, MNRAS, 344, 887
Serjeant, S., et al. 2008, MNRAS, 386, 1907
Severgnini, P., et al. 2000, A&A, 360, 457
Seymour, N., Huynh, M., Dwelly, T., Symeonidis, M., Hopkins, A., McHardy, I. M., Page, M. J., & Rieke, G. 2009, MNRAS, 398, 1573
Siringo, G., et al. 2009, A&A, 497, 945
Smail, I., Ivison, R. J., & Blain, A. W. 1997, ApJ, 490, L5
Smolčić, V., et al. 2011, ApJ, 731, L27
Smolčić, V., et al. 2012, A&A, in press (arXiv:1205.6470)
Swinbank, A. M., Smail, I., Chapman, S. C., Blain, A. W., Ivison, R. J., & Keel, W. C. 2004, ApJ, 617, 64
Walter, F., et al. 2012, Nature, 486, 233
Wang, W.-H., Barger, A. J., & Cowie, L. L. 2009, ApJ, 690, 319
Wang, W.-H., Cowie, L. L., & Barger, A. J. 2004, ApJ, 613, 655 (W04)
Wang, W.-H., Cowie, L. L., & Barger, A. J. 2006, ApJ, 647, 74
Wang, W.-H., Cowie, L. L., Barger, A. J., Keenan, R. C., & Ting, H.-C. 2010, ApJS, 187, 251
Wang, W.-H., Cowie, L. L., Barger, A. J., & Williams, J. P. 2011, ApJ, 726, L18
Wang, W.-H., Cowie, L. L., van Saders, J., Barger, A. J., & Williams, J. P. 2007, ApJ, 670, L89
Wardlow, J. L., et al. 2011, MNRAS, 415, 1479
Webb, T. M., et al. 2003, ApJ, 587, 41
Weiß, A., et al. 2009, ApJ, 707, 1201
Williams, R. E., et al. 1996, AJ, 112, 1335
Wilson, G. W., et al. 2008, MNRAS, 386, 807
Wold, I. G. B., Owen, F. N., Wang, W.-H., Barger, A. J., & Keenan, R. C. 2012, ApJS, 202, 2
Younger, J. D., et al. 2007, ApJ, 671, 1531
Younger, J. D., et al. 2008, MNRAS, 387, 707
Younger, J. D., et al. 2009, ApJ, 704, 803
Yun, M. S., Reddy, N. A., & Condon, J. J. 2001, ApJ, 554, 803
Yun, M. S., et al. 2012, MNRAS, 420, 957

## APPENDIX

We present the SMA and multiwavelength images of the SMA sample in Figure A1. GOODS 850-11 (GN12) and GOODS 850-13 (GN21) were already published in Wang et al. (2011), and GOODS 850-1 (GN14/HDF850.1) in Cowie et al. (2009).

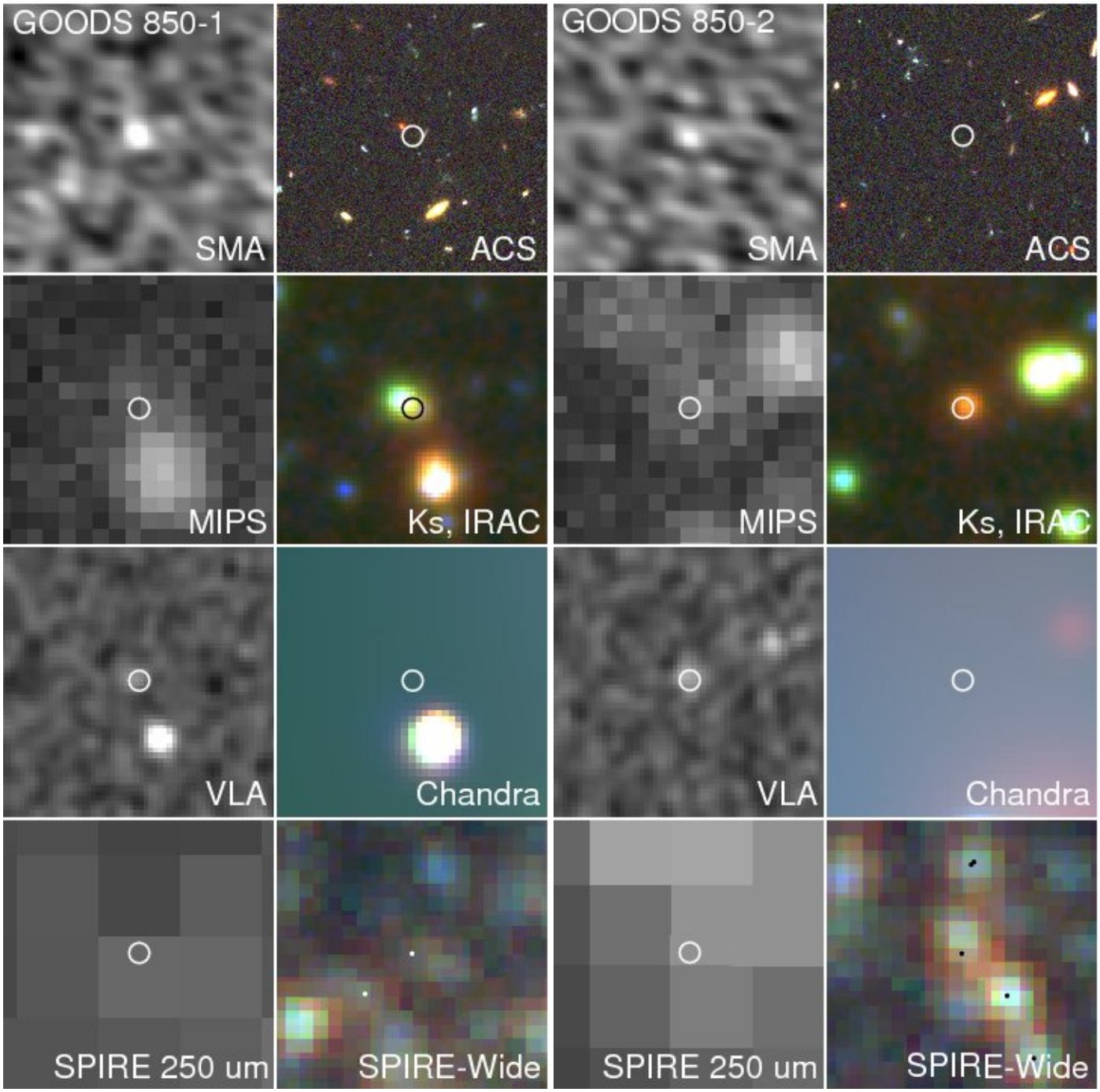



FIG. A1.— Ultradeep multiwavelength images of the SMA sample. The SPIRE-wide panels (bottom rows right) are 200″ on a side, while all of the remaining panels are 20″ on a side, except for GOODS 850-11 and GOODS 850-13, where all of the remaining panels are 25″ on a side. The small circles marking the SMA positions have diameters of 1.5″. We show them in either black or white for clarity. For each source, we show the SMA 860 $\mu$m image (top rows left); a false-color optical panel made with *HST* ACS F435W (blue), F606W (green), and F775W+F850LP (red) images (top rows right); the MIPS 24 $\mu$m image (second rows left); a false-color infrared image made with CFHT $K_S$ (blue; Wang et al. 2010), IRAC 3.6+4.5 $\mu$m (green), and IRAC 5.8+8.0 $\mu$m (red) images (second rows right); the VLA 20 cm image from Owen13 (third rows left); a false-color X-ray image made with adaptively smoothed *Chandra* $4-8$ keV (blue), $2-8$ keV (green), and $0.5-2$ keV (red) images (Alexander et al. 2003b) (third rows right); the SPIRE 250 $\mu$m image (bottom rows left); and a wide-field (200″) color image of the SPIRE 250, 350, and 500 $\mu$m data from the HerMES survey of Oliver et al. (2012) (bottom rows right). All of the SMA sources contained in each wide-field SPIRE image are marked with dots.

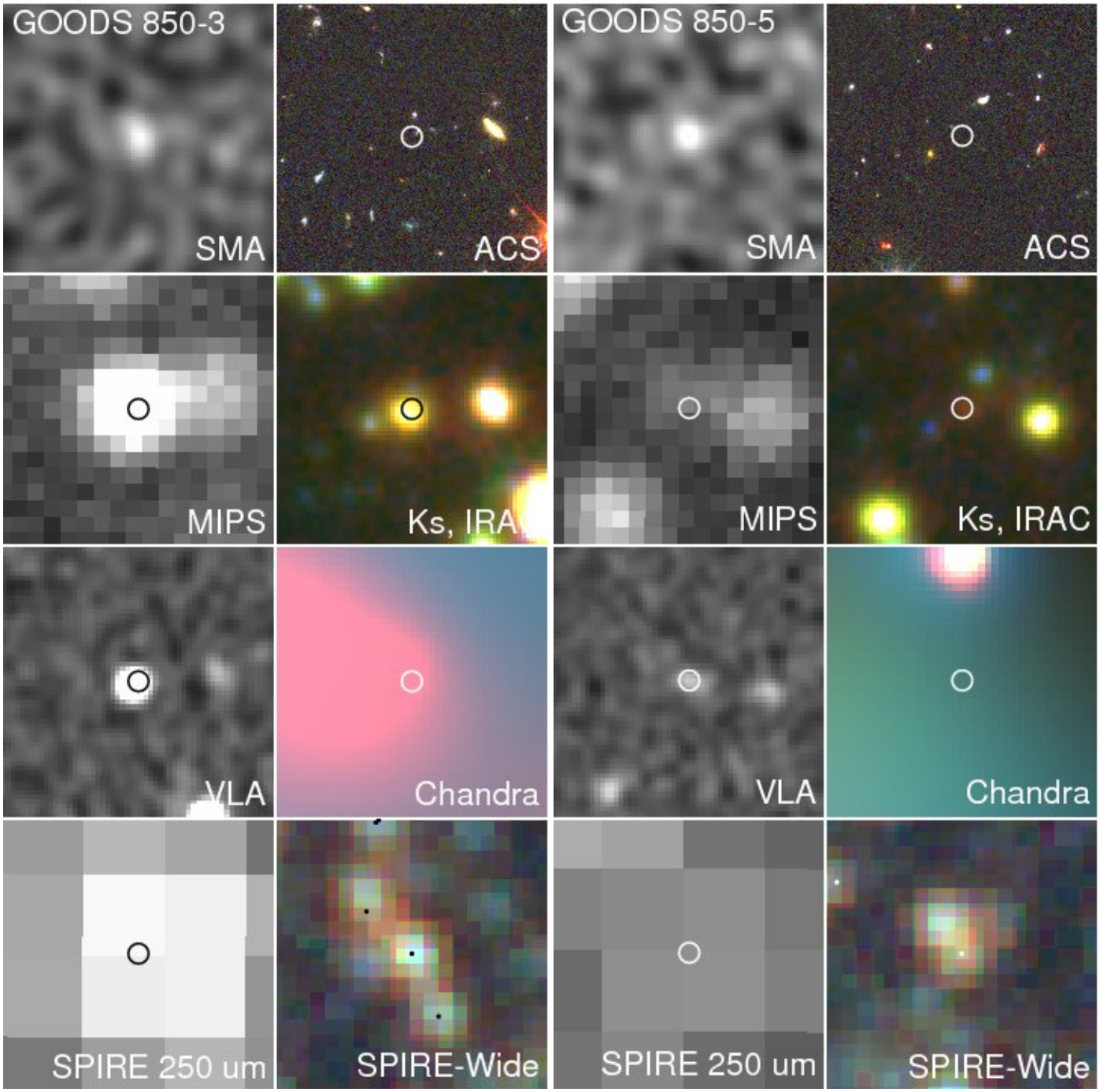

GOODS 850-3
SMA
ACS
GOODS 850-5
SMA
ACS
MIPS
Ks, IRA
MIPS
Ks, IRAC
VLA
Chandra
VLA
Chandra
SPIRE 250 um
SPIRE-Wide
SPIRE 250 um
SPIRE-Wide

FIG. A1.— CONT.

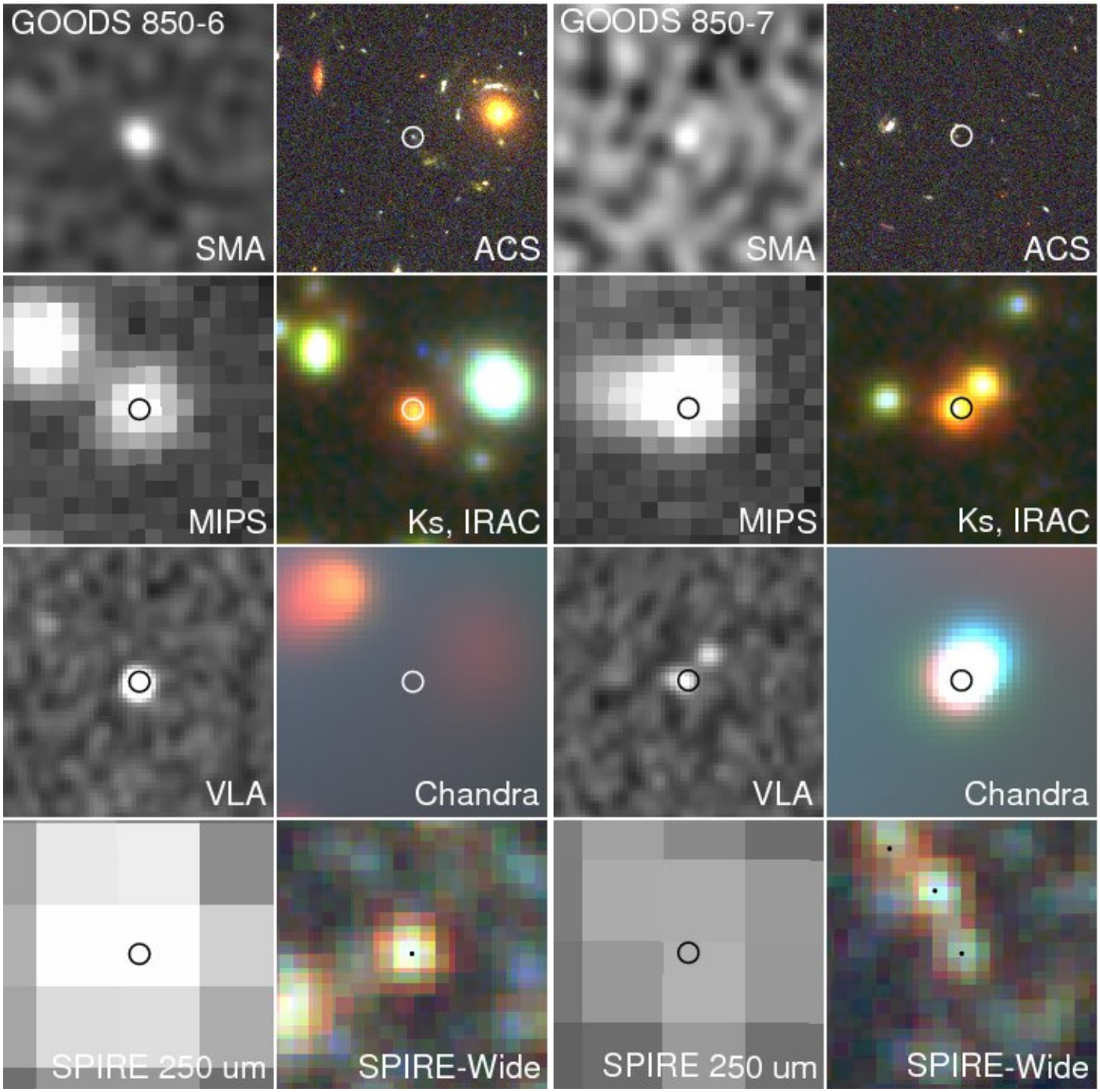

GOODS 850-6
SMA
ACS
GOODS 850-7
SMA
ACS
MIPS
Ks, IRAC
MIPS
Ks, IRAC
VLA
Chandra
VLA
Chandra
SPIRE 250 um
SPIRE-Wide
SPIRE 250 um
SPIRE-Wide

FIG. A1.— CONT.

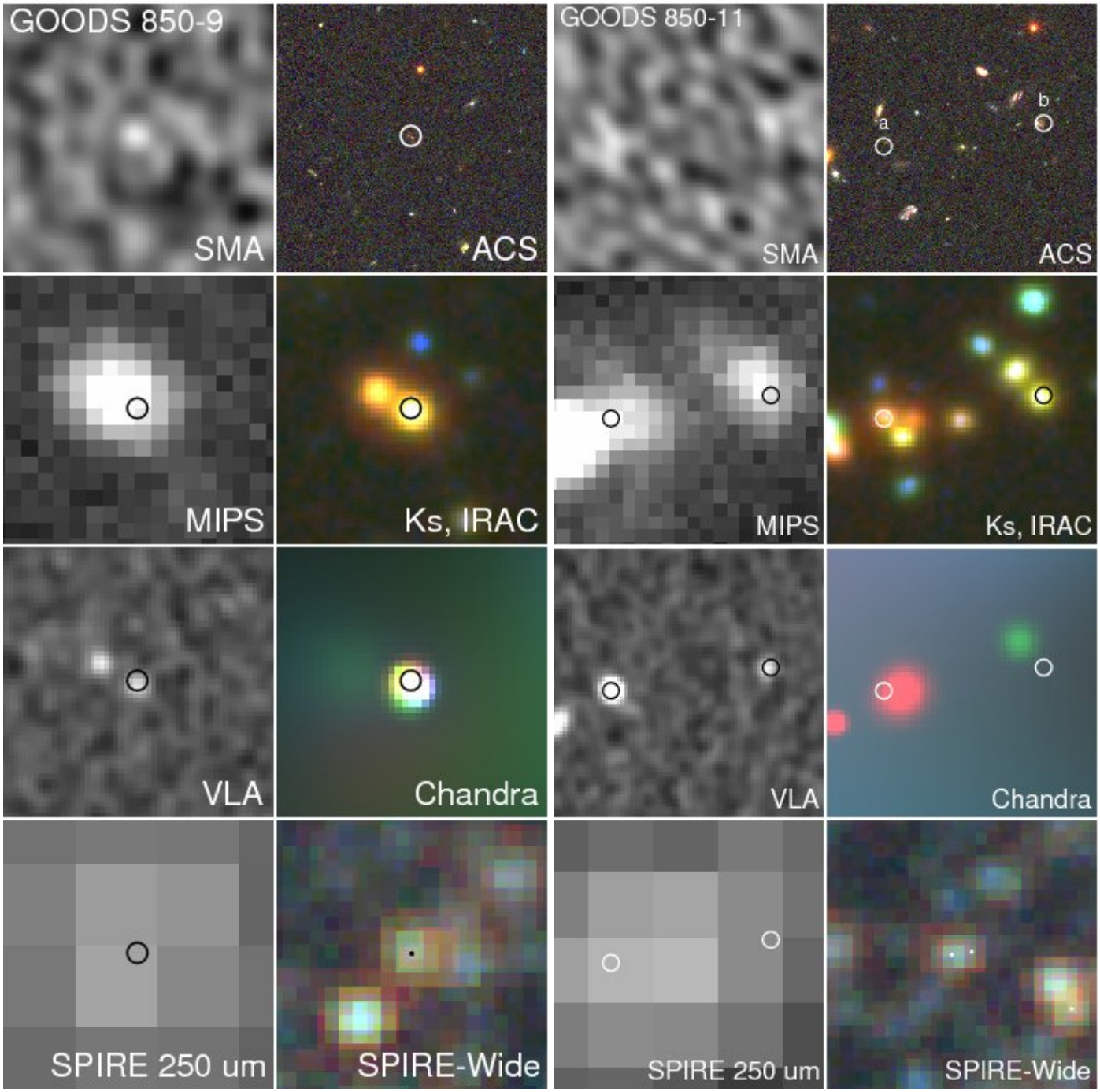

GOODS 850-9
SMA
ACS
GOODS 850-11
SMA
a
b
ACS
MIPS
Ks, IRAC
MIPS
Ks, IRAC
VLA
Chandra
VLA
Chandra
SPIRE 250 um
SPIRE-Wide
SPIRE 250 um
SPIRE-Wide

FIG. A1.— CONT.

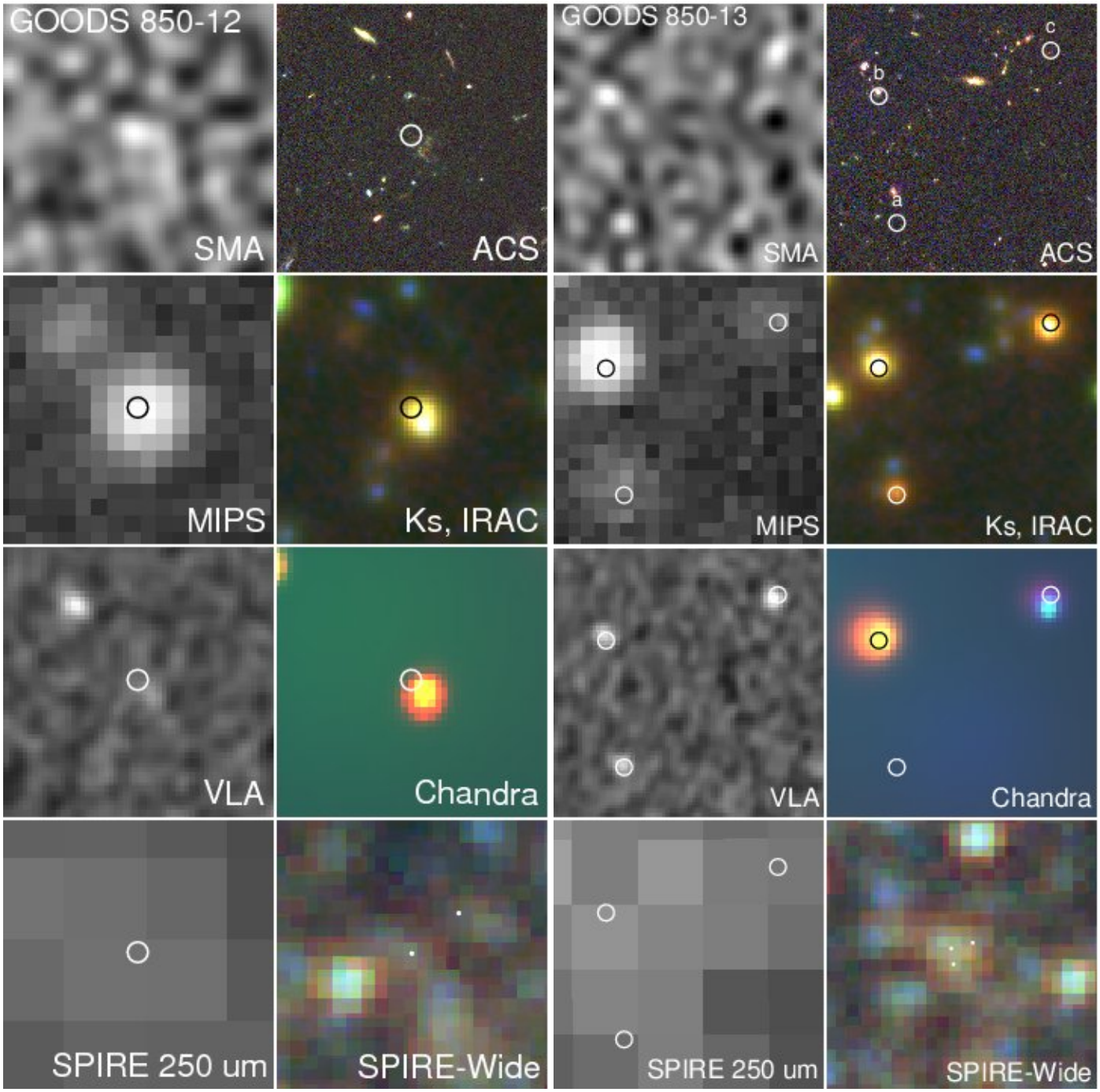

GOODS 850-12
SMA
ACS
GOODS 850-13
SMA
c
b
a
ACS
MIPS
Ks, IRAC
MIPS
Ks, IRAC
VLA
Chandra
VLA
Chandra
SPIRE 250 um
SPIRE-Wide
SPIRE 250 um
SPIRE-Wide

FIG. A1.— CONT.

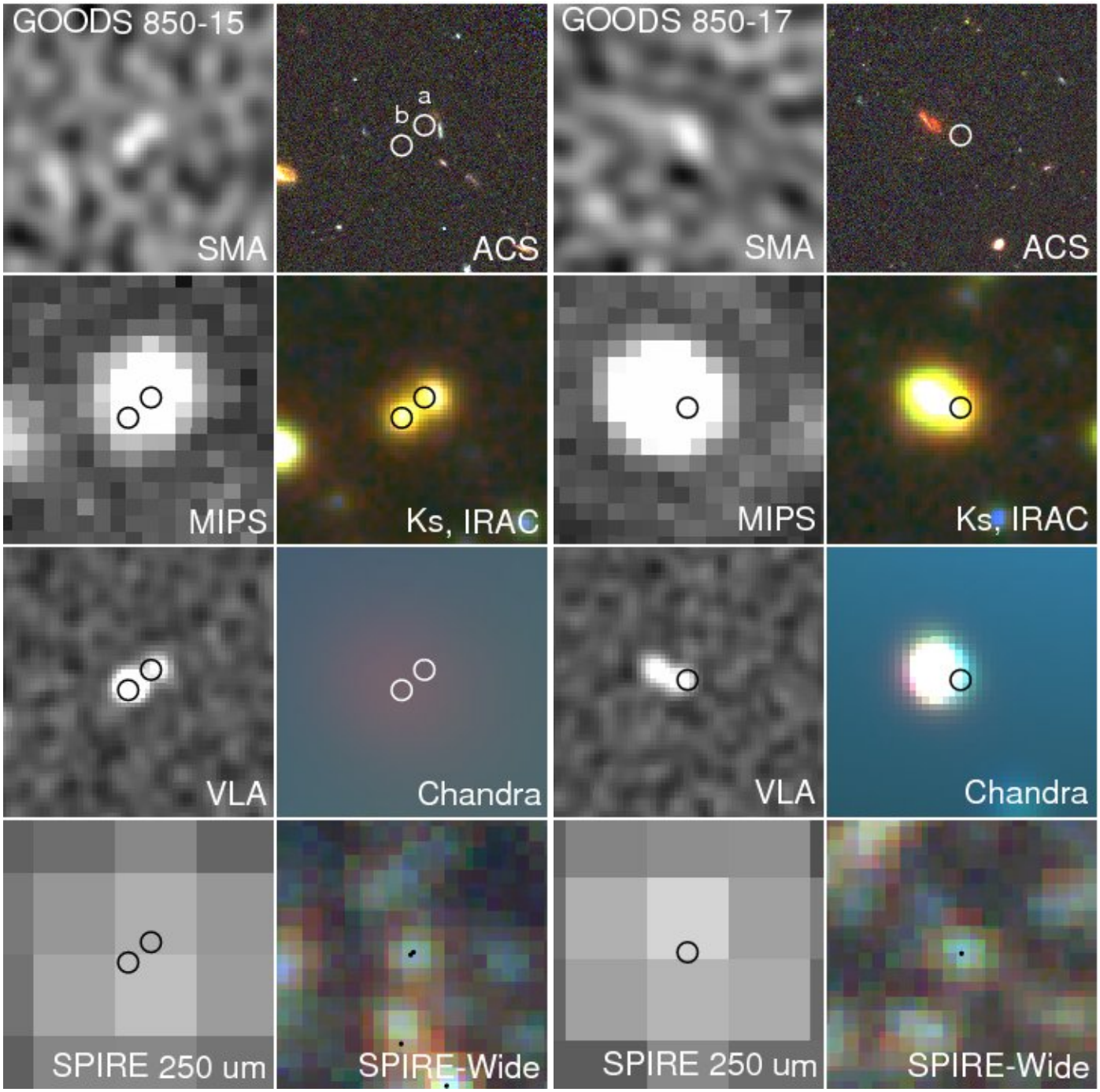

GOODS 850-15
SMA
a
b
ACS
GOODS 850-17
SMA
ACS
MIPS
Ks, IRAC
MIPS
Ks, IRAC
VLA
Chandra
VLA
Chandra
SPIRE 250 um
SPIRE-Wide
SPIRE 250 um
SPIRE-Wide

FIG. A1.— CONT.